

THE OUTER DISKS OF EARLY-TYPE GALAXIES. I. SURFACE-BRIGHTNESS PROFILES OF BARRED GALAXIES

PETER ERWIN^{1,2}

Max-Planck-Institut für extraterrestrische Physik, Giessenbachstrasse, 85748 Garching, Germany

AND

MICHAEL POHLEN

Astronomical Institute, University of Groningen, PO Box 800, NL-9700 AV Groningen, The Netherlands

AND

JOHN E. BECKMAN³

Instituto de Astrofísica de Canarias, C/ Via Láctea s/n, 38200 La Laguna, Tenerife, Spain

To appear in The Astronomical Journal

ABSTRACT

We present a study of 66 barred, early-type (S0–Sb) disk galaxies, focused on the disk surface brightness profile outside the bar region, with the aim of throwing light on the nature of Freeman Type I and II profiles, their origins, and their possible relation to disk truncations. This paper discusses the data and their reduction, outlines our classification system, and presents *R*-band profiles for all galaxies in the sample, along with their classifications. In subsequent papers, we will explore the structure of outer disks as revealed by these profiles, and investigate their possible origins.

The profiles are derived from a variety of different sources, including the Sloan Digital Sky Survey (Data Release 5). For about half of the galaxies, we have profiles derived from more than one telescope; this allows us to check the stability and repeatability of our profile extraction and classification. The vast majority of the profiles are reliable down to levels of $\mu_R \approx 27$ mag arcsec^{−2}; in exceptional cases, we can trace profiles down to $\mu_R > 28$. We can typically follow disk profiles out to at least 1.5 times the traditional optical radius R_{25} ; for some galaxies, we find light extending to $\sim 3 \times R_{25}$. For Type I (single-exponential) profiles, this means that we can trace the exponential disk out to 6–7 scale lengths.

We classify the profiles into three main groups: Type I (single-exponential), Type II (down-bending), and Type III (up-bending). The frequencies of these types are approximately 27%, 42%, and 24%, respectively, plus another 6% which are combinations of Types II and III. We further classify Type II profiles by where the break falls in relation to the bar length, and in terms of the postulated mechanisms for breaks at large radii (“classical truncation” of star formation versus the influence of the Outer Lindblad Resonance of the bar). We also classify the Type III profiles by the probable morphology of the outer light (disk or spheroid). Illustrations are given for all cases.

Subject headings: galaxies: structure — galaxies: elliptical and lenticular, cD — galaxies: spiral

1. INTRODUCTION

The radial surface brightness profiles of galaxy stellar disks are usually assumed to be exponential in nature, though it is by no means obvious that a galaxy disk *should* have an exponential profile. One of the more successful early attempts to show that an exponential disk could form naturally was by Yoshii & Sommer-Larsen (1989), who found that an exponential disk forms if the time scales for viscosity and the star formation are comparable; more recent studies along these lines include Ferguson & Clarke (2001) and Slyz et al. (2002). Although early attempts to derive exponential disks from first principles in cosmological simulations yielded disks with excess brightness in the inner profiles (e.g., Navarro & White 1994), more recent experiments in which star

formation was taken at least partially into account have been more successful (Robertson et al. 2004; Governato et al. 2007). Even so, the exponentiality of the radial brightness profile is perhaps best treated as an empirical datum.

In his pioneering paper on galaxy disks, Freeman (1970) pointed out that not all disks are simple exponentials. In particular, he identified two basic types of disk profiles: Type I, in which the disk *does* in fact show a simple exponential form; and Type II, where the outer part of the disk shows a purely exponential fall-off, but where the inner part of the profile falls below the inward projection of the outer exponential. (In both cases, the profile usually rises more steeply in the innermost part of the galaxy; this is typically assumed to represent the contribution of the central bulge.) Although it has been argued that Type II profiles are simply an illusion generated by excessive dust extinction at certain radii (Adamson et al. 1987; Phillips et al. 1991), so that the actual *stellar* profile is still Type I, the very existence of Type II profiles in S0 galaxies tends to discount this explanation. MacArthur, Courteau, & Holtzman (2003)

Electronic address: erwin@mpe.mpg.de

Electronic address: pohlen@astro.rug.nl

Electronic address: jeb@iac.es

¹ Universitäts-Sternwarte München, Scheinerstrasse 1, D-81679 München, Germany

² Guest investigator of the UK Astronomy Data Centre

³ Consejo Superior de Investigaciones Científicas, Spain

combined optical and near-IR imaging to show that dust extinction is responsible for only a subset of Type II profiles in intermediate and late-type spirals.

Another feature which is sometimes taken to be a general (or even universal) property of disks is that of a *truncation* of the stellar population at large radii, typically 2–4 exponential scale lengths (see, e.g., the review by Pohlen et al. 2004). Van der Kruit (1979) and van der Kruit & Searle (1981a,b) first drew attention to this phenomenon, which they inferred primarily from the major-axis profiles of edge-on, late-type spirals. The term “truncation” is perhaps misleading, since even the original studies did not argue for a complete absence of stars beyond the truncation radius. More recently, Pohlen et al. (2002) used deep images of three face-on spirals to show that the truncation actually takes the form of a change in slope, from the shallow exponential of the main disk to a steeper exponential at larger radii (see also de Grijs, Kregel, & Wesson 2001). From this perspective, truncations can be seen as another form of Freeman’s Type II profile, with breaks at fainter surface brightness levels than was typical of Freeman’s original sample.

Theoretical models have ascribed truncations to a feature of the initial collapsing cloud which formed the disk (van der Kruit 1987), or to the effects of a star formation threshold due to changes in the gas density or phase at large radii (Kennicutt 1989; Schaye 2004; Elmegreen & Hunter 2006). Zhang & Wyse (2000) and Ferguson & Clarke (2001) have put forward viscous evolutionary disk models which produce truncation-like features, though the latter authors argue that their truncations would tend to smooth away during the evolution of the galaxy. The influence of magnetic fields has also been proposed to account for the truncated form of disk edges (Battaner, Florido, & Jiménez-Vicente 2002), and recent N -body simulations by Debattista et al. (2006) suggest that purely stellar-dynamical effects could be a plausible mechanism.

Most of those working on explanations for truncations have implicitly assumed that all disks, or at least the great majority, are truncated. However, this appears not to be the case. At least some spirals show a single exponential brightness profile traceable out to eight or even ten scale lengths from the center, with no sign of truncation (see, e.g. Barton & Thompson 1997; Weiner et al. 2001; Bland-Hawthorn et al. 2005).

Evidence for a *third* general class of disk profiles has been presented by Erwin et al. (2005) for early-type disks and by Hunter & Elmegreen (2006) and Pohlen & Trujillo (2006) for late-type disks; an earlier identification of this phenomenon in extreme late-type spirals is that of Matthews & Gallagher (1997). In this class, dubbed “Type III” (or “antitruncation”) by Erwin et al., the inner profile is a relatively steep exponential, which gives way to a *shallower* surface brightness profile (which may or may not be exponential itself) beyond the break radius. This profile is thus something like the inverse of a Type II profile, bending “up” instead of “down” beyond the break radius. Elmegreen & Hunter (2006) showed that something like a Type III profile could result from star formation if the initial gas disk has the right (ad-hoc) radial density profile; more recently, Younger et al. (2007) argued that minor mergers can produce Type III

profiles.

Stellar disks thus seem to be a mixed and somewhat confusing bag: some disks are exponential out to very large radii, some are apparently truncated, some display classical Freeman Type II profiles (if these are indeed really distinct from truncations), and some have shallower profiles beyond a certain radius. This diversity is probably telling us something important about galaxy formation and evolution — for example, the outer part of the disk may record useful information about past accretion and interactions or the lack thereof (e.g., Ibata et al. 2005; Younger et al. 2007). It would clearly be useful, however, to have a better understanding of just how often, where, and in what fashion disks deviate from the simple exponential model.

This paper is part of a larger study focused on the outer disks of S0 and early-type spiral galaxies, complementing the study of late-type disks by Pohlen & Trujillo (2006). Our aim is to map out some of the actual complexity in galaxy disk profiles, look for patterns and order within this complexity, establish a general taxonomy for disk profiles, and ultimately attempt to understand *why* disk profiles behave the way they do. Along the way, we hope to test some recent models of star formation in galaxy disks, and lay the groundwork for more general testing of disk galaxy formation models.

Here, we present surface brightness profiles and classifications for a sample of 66 S0–Sb galaxies. These galaxies are the *barred* subset of our early-type sample (a total of 118 galaxies); the data and analysis for the unbarred galaxies will be presented in a subsequent paper (Gutiérrez et al. 2007). We concentrate first on the barred galaxies — which are the majority of the sample — because they have a unique and useful characteristic: the bar can be used as a measuring rod. As we will show below and in Erwin et al. (2007), the bar size provides a useful and informative way to analyze Type II profiles in particular, and there are hints of strong connections between the bars and the disk profiles.

The outline of this paper is as follows. In Section 2 we describe the galaxy sample, the imaging observations made, a brief description of the data taken from archives, and the reduction and photometric calibration of the images. In Section 3 we explain how we obtained the radial surface-brightness profiles of the galaxies, the comparison of the profiles made with data from different telescopes, and the quality of the profiles taken from Sloan Digital Sky Survey images. Section 4 presents the detailed classification scheme for the surface brightness profiles, with illustrative examples. Finally, in Section 5 we show individual profiles for all the galaxies and supply explanatory notes for individual galaxies.

2. SAMPLE AND OBSERVATIONS

2.1. The Sample

Our sample is essentially the same as that presented in Erwin (2005), which in turn was an expansion of a sample originally studied by Erwin & Sparke (2003). The expanded sample consists of all galaxies from the Uppsala General Catalog (Nilson 1973) which are nearby (heliocentric redshift ≤ 2000 km s $^{-1}$), northern ($\delta > -10^\circ$), and large (diameters $\geq 2.0'$), with Hubble types S0–Sb, and strong or weak bars (SB or SAB bar types from de Vaucouleurs et al. 1991, hereafter RC3). Because of un-

certainties about how consistent Hubble types for spirals are between the Virgo Cluster and the field (e.g., van den Bergh 1976; Koopmann & Kenney 1998), we excluded Virgo Cluster spirals (but retained the S0 galaxies). We also removed nine galaxies which did not appear to have bars, despite their SB or SAB classification, or which were involved in strong interactions; see Erwin (2005).

The trimmed sample has a total of 66 galaxies. This is one more than the sample presented in Erwin (2005) because inspection of an *H*-band image from the Galaxy On Line Database Milano Network (Gavazzi et al. 2003)⁴ shows that NGC 4531 *is* in fact barred, though Erwin had described it as unbarred based on available optical images. The galaxies and their global properties are listed in Table 1.

As mentioned above, the sample is restricted to barred galaxies. Because we include galaxies with both strong and weak bars, we cover at least two-thirds of local disk galaxies (e.g., Eskridge et al. 2000; Laurikainen et al. 2004; Menéndez-Delmestre et al. 2007; Erwin 2007a). We also have images for the corresponding *unbarred* galaxy sample, which are currently being analyzed (Aladro et al. 2007). Details of their surface-brightness profiles and similarities with (or differences from) the barred galaxies will be discussed in future papers (Gutierrez et al. 2007).

2.2. Observations

The field S0–Sa galaxies in our sample were previously studied by Erwin & Sparke (2002, 2003), who imaged almost all of them in *B* and *R* with the 3.5m WIYN Telescope. Subsequently most of the Sab and Sb galaxies, as well as the Virgo S0 galaxies, were imaged in *B* and *R* with the Andalucia Faint Object Spectrograph and Camera (ALFOSC) on the Nordic Optical Telescope (NOT) in 2001 and 2002.

Unfortunately, the majority of these images turned out not to be useful for the present study, for two reasons. First, the small fields of view of the imagers ($6.8' \times 6.8'$ for WIYN and $6.4' \times 6.4'$ for NOT/ALFOSC) meant that the outer disks of many of our galaxies filled most of the CCDs. We have found that light from the stellar disks can often be traced to at least *twice* the RC3 D_{25} diameter. Since all of our galaxies have, due to the way the sample is defined, $D_{25} \geq 2'$, each galaxy's disk thus extends to at least $4'$ in at least one dimension; galaxies with $D_{25} > 3'$ will essentially fill the CCD in at least one dimension (in both dimensions if the galaxy is close to face-on). This means that there is often little or no area on the image where the sky background can be measured.

Second, many of the images proved to have significant scattered light problems, which manifest as backgrounds which are not flat at large distances from the galaxy. From comparison with images having a larger field of view (see below), we suspect that the problematic WIYN images are usually affected by scattered light from nearby bright stars; images where this was not the case (and where the galaxy was relatively small) were still usable. On the other hand, the NOT/ALFOSC images routinely showed large-scale variations out to the borders of the images, even when there were no bright stars in the vicinity. In this case, we suspect that scattered light from the galaxy itself is the culprit, in part

because the pattern of excess light seems to match the orientation of the more elongated galaxies, and because the effect seemed to be independent of lunar phase.

To remedy this problem, we turned to images obtained with the Wide Field Camera (WFC) of the 2.5m Isaac Newton Telescope (INT). These were taken during two observing runs: 2003 September 19–21 and 2004 March 14–17. Conditions were photometric on the first night of the 2003 run and on all four nights of the 2004 run. Seeing varied from 1.0 – $1.5''$ in the 2003 run and from 0.7 – $3.4''$ during the 2004 run; poor seeing is *not* a problem for our analysis, since we are interested primarily in the outer disks, where we must average the light over large spatial areas.

For four more galaxies, we were able to retrieve usable images from the Isaac Newton Group (ING) archives; these were taken either with the INT-WFC, the earlier Prime Focus Camera Unit on the INT, or with the 1m Jacobus Kapteyn Telescope (JKT). Additional image sources included the BARS Project (Lourenso & Beckman 2001) for NGC 4151 and 4596, and the catalog of Frei et al. (1996) for NGC 5701. For NGC 4612, we made use of *R*-band images from the 2.4m MDM Telescope at Kitt Peak (1996 March, courtesy Paul Schechter).

Finally, we found images for about three quarters of our sample in the Sloan Digital Sky Survey (York et al. 2000), including Data Release 5 (Adelman-McCarthy et al. 2007). This provided an additional source of comparison for galaxies already observed, as well as images of *better* quality for 22 galaxies (mainly because the sky background in the SDSS images tended to be very uniform). The reduced images were retrieved from the SDSS archive; in cases where a galaxy extended off the top or bottom of a given field, we retrieved the adjacent field(s) from the same scan and merged them to create larger images including as much of the galaxy as possible. Adjacent SDSS fields are sequential products of a given observing run and so can be merged without fear of significant changes in orientation or observing conditions, though secular changes in the sky background can show up as vertical gradients.

Table 3 lists the primary and secondary images used for each galaxy. The first (and sometimes only) image is what we used to extract the surface-brightness profile; if another image was useful (e.g., for photometric calibration or validation of the surface-brightness profile shape), it is listed afterwards.

2.3. Reduction

The reduction of images taken with the WIYN Telescope has already been discussed by Erwin & Sparke (2003). Here, we focus on those images taken with the INT-WFC, MDM, NOT, and the archival ING images.

All images were reduced using standard tools and techniques within IRAF, including bias subtraction and flat fielding. During our first set of INT-WFC observations (2003 September), we obtained both dome flats and twilight flats. Test reductions using both sets of flat fields showed that the twilight flats produced significantly flatter backgrounds, so we used twilight flats for those and all subsequent INT-WFC reductions.

For all of the galaxies observed with the INT-WFC, the central CCD (Chip 4) was large enough to include both the galaxy and a significant amount of sky around

⁴ available online at <http://goldmine.mib.infn.it/>

it, so we reduced the Chip 4 images in isolation and did not attempt to construct full image mosaics. Although the WFC suffers from strong optical distortions near the edges of its field, the center of Chip 4 is close to the optical axis, so galaxy isophotes on that chip are not significantly affected.

Multiple exposures were typically offset by only 10–20", so we aligned them prior to coadding with simple linear shifts; the shifts were calculated using positions of stars near each galaxy.

2.3.1. Sky Subtraction

Proper sky subtraction is essential for deriving accurate surface brightness profiles, since under- or over-subtraction can introduce false curvature or obscure existing curvature.

We inspected all images for the existence of 2D structure in the sky background by generating median-smoothed copies of each image. Isolated, small-scale structures (e.g., dust-grain halos not removed by flat-fielding) were masked out, but large-scale gradients, including occasional vertical gradients in SDSS images, were removed using the IRAF `imurfit` routine. Regions for the fit were selected to be both far from the galaxy and free of contamination by bright stars. We usually fit the background with a linear function, but occasionally higher-order polynomials were needed.

The main stage of sky subtraction was the determination of the mean sky background level, including the level in the residual images which resulted from `imurfit` processing. The method we used involved measuring the median level in 10×10 pixel boxes in regions devoid of bright stars and scattered light, located well outside the galaxy. Since, as we show below, stellar light can often be traced out to at least twice R_{25} , we were careful to measure the sky background only in regions farther away from the galaxy. The number of regions sampled depended on the image size and the area that was free of bright stars, neighboring galaxies, etc., but ranged between 40 and 100. The final sky level was the mean of these 40–100 median values.

The advantage of measuring the sky background this way is twofold. First, we were able to avoid sampling regions that contain galaxy light or scattered light from bright stars (the latter were identified by inspection of median-filtered copies of the images). Second, it enabled us to compute an estimate of our uncertainty by bootstrap resampling: we re-computed the mean from a re-sampled set of the median values 500 times, and took the standard deviation of these 500 estimates as our uncertainty σ_{sky} . A possible disadvantage of our technique is that we may occasionally underestimate the sky background for the galaxy itself if there are patches of scattered light within the galaxy-dominated part of the image, though we do mask bright stars within the galaxy when we do our ellipse fitting.

A more ideal method for both estimating the background level and the uncertainty thereof might be that used by Barton & Thompson (1997) and Pohlen & Trujillo (2006). In this approach, concentric fixed ellipses are used to determine the intensity level as a function of radius from the galaxy center. By extending this to well outside the galaxy, the intensity will asymptotically approach the background level; variations from one annulus

to the next can be used to determine the uncertainty on the background estimate. Unfortunately, this requires an image which is both very large (with the galaxy well centered) and very uniform, whereas a significant number of our images are either not large enough in both dimensions or contain regions affected by scattered light, or both. But a comparison of background and σ_{sky} estimates for 8 SDSS images measured using both methods shows that the background measurements typically differ by less than $1.5\sigma_{\text{sky}}$, and the σ_{sky} values themselves agree to within 10%.

Following Pohlen & Trujillo (2006), we use the sky uncertainty σ_{sky} to define a “critical” surface brightness level below which we consider our profiles to be uncertain. We do this by setting $\mu_{\text{crit}} = 4.94\sigma_{\text{sky}}$, which corresponds to the level at which a $1\text{-}\sigma$ error in the sky subtraction would shift the profile by $0.2\text{ mag arcsec}^{-2}$ (see the bottom panel of Fig. 2 in Pohlen & Trujillo). This level is indicated on our profile plots by a horizontal dashed line. For the majority of our profiles, $\mu_{\text{crit}} \sim 26.5\text{--}27$ in R , but fainter levels exist: there are seven galaxies with $\mu_{\text{crit}} \gtrsim 28\text{ mag arcsec}^{-2}$.

2.4. Photometric Calibration

With three exceptions, all of our images and surface brightness profiles are calibrated to Cousins R , either directly via observations of standard stars or the use of published aperture photometry, or indirectly via conversion of SDSS zero points from r to R . The exceptions — NGC 1022, NGC 4319, and UGC 11920 — were cases where none of our images were obtained during photometric conditions, and for which we could find no literature calibrations. Although we used the SDSS r filter for many of our own observations (to reduce the possibility of fringing in the sky background), we opted to calibrate all images to Cousins R .

Our images come from a variety of sources, and we used a variety of methods to calibrate them. The largest set was the direct calibration of our 2003 September and 2004 March INT-WFC observations via standard-star observations made during the same night. For other images, we did the calibrations using short exposures from the photometric INT-WFC runs, aperture photometry from the literature, or SDSS images, as explained below.

2.4.1. INT-WFC Photometric Observations

The first night of our 2003 September run at the INT, and all four nights of our 2004 March run, were photometric. Standard stars from Landolt (1992) fields were observed in both B and r filters throughout each photometric night.⁵ The photometric calibration was then done by fitting following equations using the `fitparams` task from the IRAF photcal package:

$$B_{\text{inst}} = B - Z_B + k_{1,B}X + k_{2,B}(B - R) \quad (1)$$

$$R_{\text{inst}} = R - Z_R + k_{1,R}X + k_{2,R}(B - R) \quad (2)$$

where the instrumental magnitudes are B_{inst} and R_{inst} , the catalog magnitudes from Landolt (1992) are B and R , the zero points are Z_B and Z_R , and X is the airmass.

For the R -band calibrations we used a fixed extinction term $k_{1,R}$ taken from the Carlsberg Meridian Telescope’s

⁵ The exception is the first night of the 2004 March run, when no B -band observations were made.

nightly extinction measurements.⁶ We proceeded by first determining color terms (k_2) for each night. We then derived mean color terms for the entire run and then re-determined the zero points (Z_B and Z_R) using the fixed color terms. The final values are given in Table 2.

Proper calibration of individual galaxy images using the coefficients derived above requires knowing a galaxy’s $B-R$ color. For some of the galaxies, we used large-aperture colors from the compilation of Prugniel & Heraudeau (1998); for others, we determined $B-R$ colors from large-aperture photometry on our B and r images, iterating until the color values converged. However, for the majority of galaxies observed with the INT-WFC, we were unable to find or derive individual $B-R$ colors, so we assumed the following default colors based on Hubble type: $B-R = 1.5$ for S0, $B-R = 1.4$ for S0/a and Sa, and $B-R = 1.3$ for Sb. These values are based on the calibrated colors of other galaxies in our sample, as well as additional unbarred galaxies observed during the same INT-WFC observing runs. Since an error of 0.1 in $B-R$ translates to a zero-point change of less than 0.01 mag, our calibrations are not strongly affected by uncertainties in galaxy colors.

For four galaxies observed with the INT-WFC under photometric conditions (plus three additional galaxies not in this barred-galaxy sample), we found aperture magnitudes in the literature (Prugniel & Heraudeau 1998). We used these to test the accuracy of our standard-star calibrations; the results indicate that our calibrations agree with literature photometry to within 0.1 magnitudes, and usually to better than 0.05 magnitudes.

Because most of the previous observations with the WIYN Telescope were made under non-photometric conditions, we also observed several of these S0–Sa galaxies with the INT-WFC during the 2004 March run, usually with very short (30–120s) exposures. These were used to calibrate the pre-existing deeper exposures from the WIYN Telescope, by matching surface brightness profiles derived from the WIYN and INT images using the same fixed-ellipse-fit parameters. (While it is also possible to calibrate the images by performing matching aperture photometry, several of the deep WIYN images were saturated in the galaxy center.) We also used this approach to calibrate a deep image of NGC 6654 from a non-photometric night of our 2003 September INT-WFC run.

For NGC 2787, we used archival JKT observations (from 2001 January 29) of NGC 2787 to calibrate our WIYN image of the galaxy. The JKT observations, originally made by Edo Noordermeer, were obtained under photometric conditions, and were accompanied by observations of Landolt standards. Because the standard star observations covered only a limited range of airmass, we used the r -band extinction measurement from the Carlsberg Meridian Telescope observations. The WIYN image was calibrated by matching aperture photometry performed on the WIYN image to that performed on the calibrated JKT images.

2.4.2. Calibration of Images Using Aperture Photometry

Other galaxy images were calibrated using aperture photometry from the compilation of Prugniel & Heraudeau (1998); these are marked with “PH98” in column 6 of Table 3. We used the `apphot` task from the `digiphot` package of IRAF to perform aperture photometry on our sky-subtracted images, using apertures of the same sizes as in the literature (we did not use data from apertures with diameters smaller than $20''$, in order to minimize possible problems from differences in seeing or centering between our measurements and those in the literature). The instrumental magnitudes were compared with the literature values to derive appropriate zero points for the images. For NGC 4699 and NGC 7743, the only red photometry in Prugniel & Heraudeau (1998) is the aperture photometry of Sandage & Visvanathan (1978), which uses their own r filter (*not* the same as the SDSS r filter); we used their conversion of $V-r$ to $V-R$. Since it is not clear if the “ R ” in this conversion corresponds to Johnson R or Cousins R , and because there has apparently been little or no follow-up calibration of this filter system, the calibrations for NGC 4699 and NGC 7743 should be considered more uncertain than those of other galaxies.

2.4.3. Calibration using SDSS Images

For five galaxies, we used profiles from non-SDSS images but calibrated them using SDSS images, as follows. We measured $g-r$ colors in large apertures centered on the galaxies in the SDSS images (large enough to encompass most of the galaxy while still staying within the image boundaries), and used these colors to convert the SDSS r -band zero points (derived from the headers of the `tsField` files accompanying each field) to Cousins R . The conversion used Table 7 of Smith et al. (2002), so that the Cousins R magnitude is

$$R = r - 0.14(g - r) - 0.14. \quad (3)$$

The non-SDSS images were then calibrated using matching aperture photometry.

Finally, there were 22 galaxies for which we used profiles derived directly from SDSS images. The SDSS r -band zero points were converted to Cousins R as we have just described.

3. THE PROFILES

In this study we are primarily interested in the question *What are the radial surface-brightness profiles of stellar disks?* There are several related questions, such as: *Where and how often are stellar disks truncated? What form does a truncation take? Are features such as bars, rings, and spiral arms simply azimuthal redistributions of the underlying exponential disk?* For all of these questions, a key first step is to determine the mean surface brightness as a function of radius.

Another reason that the mean (i.e., azimuthally averaged) surface-brightness profiles are important is their potential for testing models of disk formation and evolution. Current models for the formation of exponential disks (e.g., Ferguson & Clarke 2001; Slyz et al. 2002), as well as for such features as disk truncations or antitruncations (e.g., Battaner, Florido, & Jiménez-Vicente 2002; Schaye 2004; Elmegreen & Hunter 2006; Debattista et al. 2006; Younger et al. 2007), are almost all strictly one-dimensional.

⁶ http://www.ast.cam.ac.uk/~{dwe}/SRF/camc_extinction.htm

To obtain our profiles, we used of the IRAF task `ellipse`. It is important to distinguish between two related uses of this and other routines which fit ellipses to galaxy isophotes. The more general fitting is with “free” ellipses, where the ellipse position angle (PA) and ellipticity are allowed to vary (as well as, optionally, the ellipse centers). In contrast, one can also fit using “fixed” ellipses, where the ellipse center, PA, and ellipticity are held fixed, and only the semi-major axis and intensity are allowed to vary. If the ellipse shape and orientation are matched to that of the projected galaxy disk, then this is (almost) equivalent to averaging on concentric circles for a face-on galaxy. (There will be differences if parts of the galaxy, such as its bulge, are not flat, or if the disk is very thick and the galaxy is highly inclined.)

Even though free-ellipse fits are often used to generate surface brightness profiles for galaxies, there *can* be significant differences between profiles generated with free ellipses and profiles generated with fixed ellipses. Figure 1 shows the different profiles produced by free-ellipse and fixed-ellipse fits for the same image, in this case an artificial galaxy consisting of an exponential disk with, at $r < 200$ pixels, a bar which is a purely azimuthal redistribution of the underlying disk:

$$I(r, \theta) = I_0 \exp(-r/h) \cos(2\theta). \quad (4)$$

The fixed-ellipse fit (solid line) recovers the underlying exponential profile, as we would expect. However, the free-ellipse-fit profile (dashed line) differs in the bar region, because the ellipses alter shape to track the bar-distorted isophotes. A possible real-world example of this phenomenon is shown in Figure 2 for the galaxy NGC 4665.

An additional reason for using fixed-ellipse fits is the fact that at large radii the S/N becomes so low that the free-ellipse fitting algorithm fails to converge, and the `ellipse` program automatically switches to fixed ellipses for larger radii. In this case `ellipse` uses the outermost successful ellipse fit as a template for larger radii, and this may not always be a good match to the true disk orientation (especially if the latter can be determined from, e.g., H I kinematics).

In order to know what ellipticity and position angle to use for the profile extraction, we of course need to know the orientation of the disk. We do this using a variety of techniques (see Erwin & Sparke 2003, Erwin 2005, and Section 5.1 for discussions of the determinations for individual galaxies), including kinematic determinations if they are available. For most galaxies, we rely on free-ellipse fits and the assumption that the outer disk (specifically, the disk *outside* any outer ring) is intrinsically circular. Note that because most of our profiles can be traced significantly further out than R_{25} , we sometimes derive outer-disk orientations which are different from those in RC3 or LEDA, which may be based on intermediate structures such as outer rings.

The final set of fixed-ellipse profiles is presented in Section 5 (Figure 14), along with comments on the individual galaxies. These profiles were generated using logarithmic radial spacing (the semi-major axis of each successive annulus is 1.03 times larger), with the actual intensity being the median of those pixels in the annulus after a sigma-clipping algorithm was applied. In all cases, background or neighboring galaxies and the halos

of bright stars were masked out; a typical example of this process can be seen in the upper panel of Figure 2 of Pohlen & Trujillo (2006), although for this study we used circular and elliptical masks to better match the shapes of galaxies and stellar halos.

3.1. Comparison of Profiles from Different Telescopes

We have usable images from at least two different telescopes for 31 of the 66 galaxies in our sample. (By “usable,” we mean that the images are large enough to have measurable sky background outside the galaxy, and the background is reasonably flat and free of complex scattered light.) This allows us to check the validity of our profiles and our profile classifications: how “repeatable” and reliable are our profiles? Figure 3 shows one such comparison, for the galaxy NGC 7280; Figure 4 shows more comparisons, concentrating on those involving SDSS images. Although small variations in the profiles at large radii are present, in almost all cases the basic shape of the profile is consistent.

3.1.1. The Quality of Profiles from SDSS Images

As noted in Section 2.2, we use profiles derived from SDSS r -band images for 22 galaxies, either because images from other telescopes suffered from small fields of view or scattered light problems, or because no other images were available. At first glance, SDSS images might not seem deep enough for reliable surface-brightness profiles of the faint outer disk ($\mu_R \gtrsim 24$); after all, the images are from a 2.5m telescope with effective exposure times of only 54 seconds.

In practice, we have found the SDSS images to be surprisingly useful: it is possible to measure reliable (azimuthally averaged!) surface brightness profiles down to at least $\mu_R \sim 26$, and often down to $\mu_R \sim 27$. Pohlen & Trujillo (2006) reached a similar conclusion in their analysis of a large sample of SDSS-derived profiles. This appears to be due to a combination of three factors: SDSS images are always taken during dark time; the images are taken in drift-scan mode, which allows for very accurate flat-fielding; and excellent telescope and camera design which significantly reduces scattered light problems (Gunn et al. 1998, 2006).

To show how reliable the profiles from SDSS images are, Figure 4 compares profiles from SDSS images with profiles from our own deeper observations (i.e., longer exposure times with similar-sized or larger telescopes). In some cases, the other images are only marginally deeper (e.g., 120s on the 2.5m INT), but in others we have combined images with cumulative exposures times of 10, 20, or even 40 minutes. As can be seen from the figure, in almost all cases the SDSS-based profiles agree very well with the profiles from deeper images. Even in cases where the profiles start to diverge at faint surface-brightness levels (e.g., NGC 3941, NGC 4037, and NGC 5338), the basic nature of the profiles are unchanged: for example, both profiles for NGC 4037 show a downward break at $r \sim 80''$, indicating a Type II profile. A similar comparison using very deep images of two galaxies from Pohlen et al. (2002) is presented in Pohlen & Trujillo (2006, their Fig. 3).

4. CLASSIFICATION OF SURFACE-BRIGHTNESS PROFILES

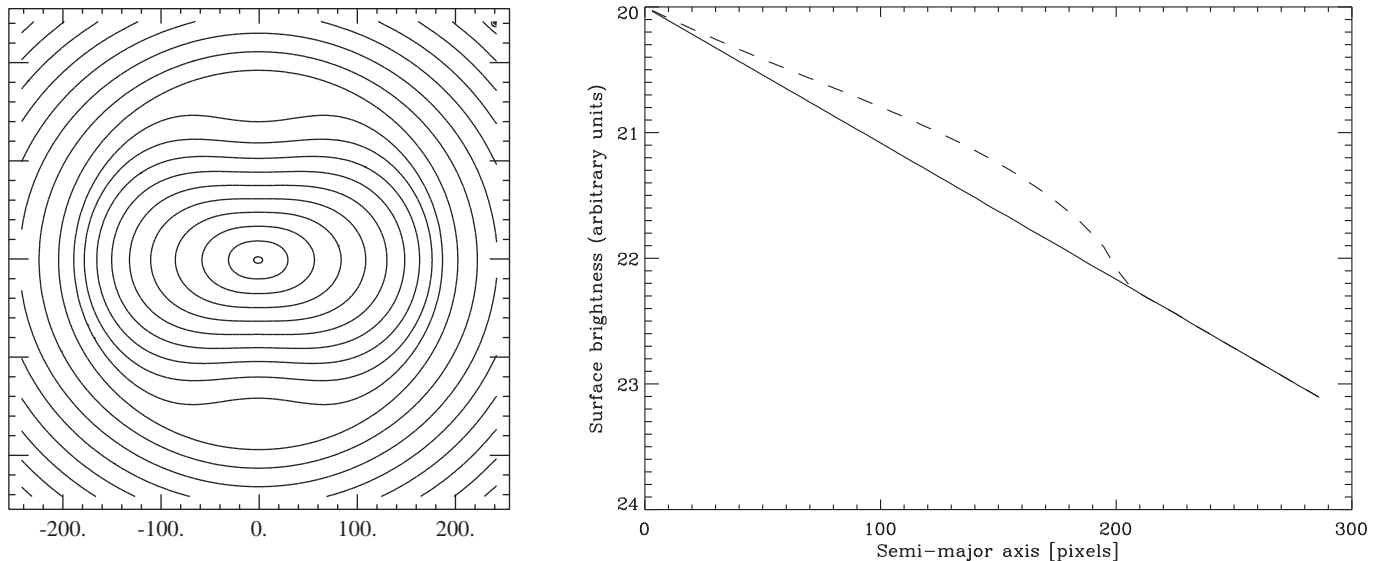


FIG. 1.— A model galaxy image (isophotes in left panel) and corresponding surface-brightness profiles (right panel) derived using fixed ellipse fits (solid line, matching the ellipticity and position angle of the outer disk) and free ellipse fits (dashed line, with ellipse position angle and ellipticity allowed to vary). The model galaxy has a bar which is a purely azimuthal ($\cos 2\theta$) perturbation (for $r < 200$ pixels) of an exponential disk. The fixed-ellipse profile recovers the true mean profile; the free-ellipse profile deviates at $r < 200$ pixels where the ellipses alter shape to trace the bar.

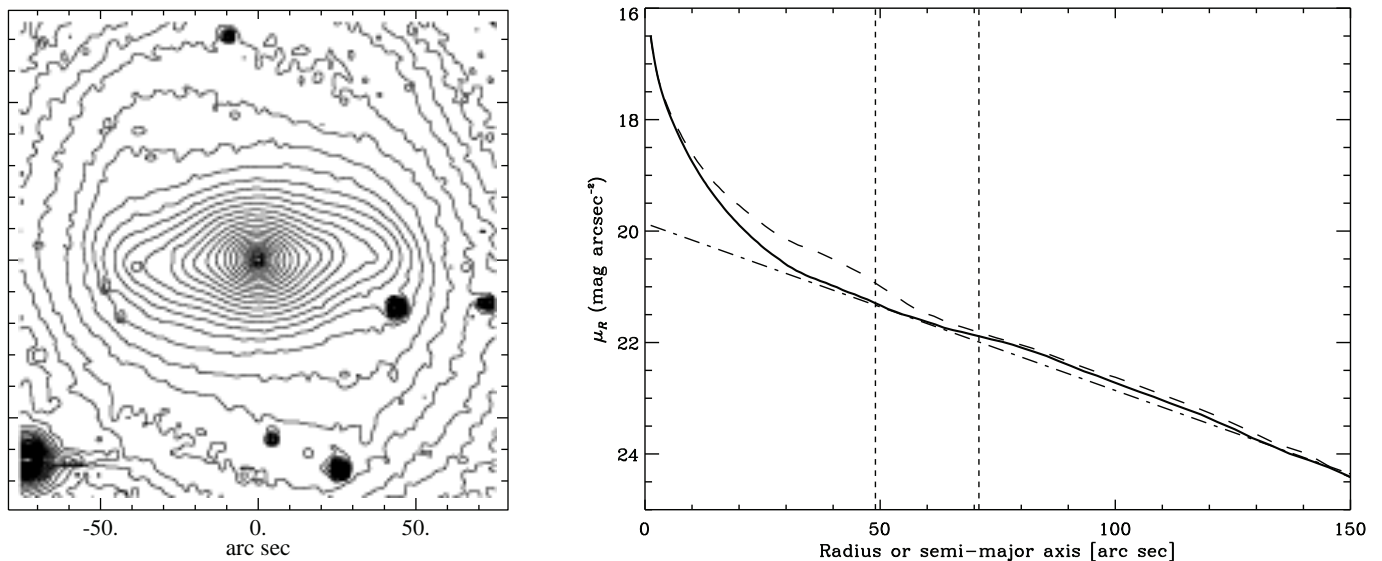


FIG. 2.— As for Figure 1, but now showing surface-brightness profiles from an r -band image of the SB0/a galaxy NGC 4665. The vertical dotted lines indicate lower and upper limits on the bar size (a_ϵ and L_{bar} from Table 1); the diagonal dot-dashed line is an exponential fit to the fixed-ellipse profile at $r = 125\text{--}179''$ (see Figure 14). The free-ellipse-fit profile (dashed line) is significantly brighter in the region $a \sim 20\text{--}70''$, due to the fact that the ellipses trace the bar.

In this section we lay out the classification scheme we have worked out for galaxy surface brightness profiles. This scheme, summarized in Figure 5, can be thought of as having three levels: a purely descriptive classification consisting of three basic types (I, II, and III); a refinement for Type II profiles based on the location of the break relative to the bar size; and a final interpretive level applied to Type II and Type III profiles. Some of this has already been discussed briefly in Erwin et al. (2005), and in more detail by Pohlen & Trujillo (2006).

The profile classifications for individual galaxies are

given in Table 4.

4.1. Basic Classifications: Types I, II and III

The first level — **Type I** vs. **Type II** vs. **Type III** — is a very general, empirical description of the profile shape outside the bar radius. This is an extension of the scheme introduced by Freeman (1970), who divided disk profiles into Types I and II. Our innovation — made possible by profiles which extend to fainter surface-brightness levels than Freeman had access to — is the identification of *Type III* profiles as a third major class

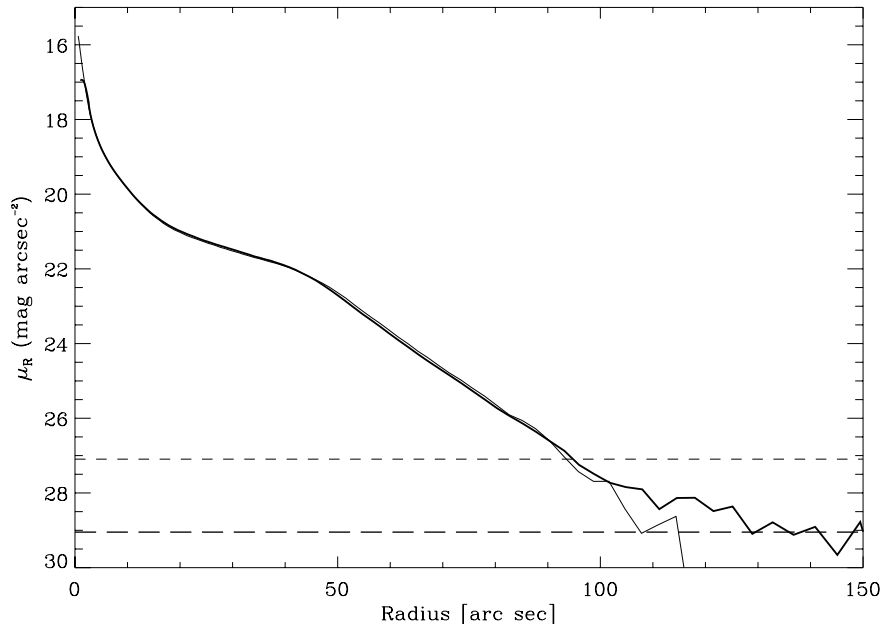


FIG. 3.— Comparison of surface-brightness profiles for NGC 7280 derived from different observations. The thick profile is from a 10200s observation with the 2.5m Isaac Newton Telescope’s Wide Field Camera, while the thin line is the profile from a 300s observation with the 3.5m WIYN Telescope. The two profiles have been scaled to match in the region $r = 5\text{--}80''$. The horizontal dashed lines mark the limiting surface brightness levels μ_{crit} for the two profiles (thick for INT-WFC profile, thin for WIYN profile).

(Erwin et al. 2005). Examples of these three basic types are given in Figure 6.

Type I profiles are single-exponential profiles, with the profile continuing out to the limit set by our sky-background uncertainty μ_{crit} .

Type II profiles contain a break, where the profile bends “down” – that is, the profile becomes steeper outside the break. In most cases, the profile is exponential both inside and outside the break, with two different slopes; in a few extreme cases, the profile inside the break is *not* exponential (e.g., NGC 2859). In some galaxies the break is quite sharp; in others it can be an extended region of gradual curvature. This class includes so-called “truncations.”

Type III profiles are similar to Type II profiles, except that the profile bends “up” beyond the break – that is, it changes from a steep exponential to something shallower at large radii. The outer part of the profile (beyond the break) is often exponential, but is sometimes curved. Again, the break is sometimes sharp and sometimes gradual. We also refer to these profiles as “antitruncations.”

4.2. Subdivisions of Type II: Type II.i and Type II.o

The next level is a subdivision of the Type II class, in which we note whether the break is an “inner” break or an “outer” break, based on where the break takes place *relative to the bar radius* (see Figure 7). A break which is located near or at the bar radius is an “inner” break, which we call **Type II.i**. A break which happens outside the bar is an “outer” break and is called **Type II.o**. This subclassification obviously depends on the galaxy having a bar whose length we can measure! In the absence of a bar, we are left with a plain “Type II” profile, as used for unbarred galaxies in Pohlen & Trujillo (2006).

4.3. Interpretive Levels for Type II and III

The final classification stage is an interpretive one, in which we attempt to say something about the *nature*, and possibly the cause, of the breaks in Type II and III profiles.

Note that the use of “(?)” after a profile classification in Table 4 means that the *last* part of the classification is uncertain. E.g., “III-s(?)” means that the profile is definitely Type III, but that the spheroid identification for the morphology of the outer light (Section 4.3.2) is uncertain.

4.3.1. Type II.o-OLR versus Type II.o-C

First, we observe that many Type II.o profiles have a break which coincides with an outer ring (see Figure 8, top panels, for an example). Even for those cases where no outer ring is visible (as in many S0 galaxies), the break occurs at $\sim 2\text{--}3$ times the bar radius, which is where outer rings are usually found (e.g., Buta & Crocker 1993). Since outer rings are generally understood to be linked to the Outer Lindblad Resonance (OLR) of bars (e.g., Buta & Combes 1996, and references therein), we call these **Type II.o-OLR** profiles (or “OLR breaks”). If the OLR link is more circumstantial – that is, if there is no outer ring seen in the galaxy, but the break is at $\sim 2\text{--}3$ times the bar radius, – then we refer to them as **Type II.o-OLR(?)** profiles. More detailed arguments for this classification will be presented in Erwin et al. (2007).

In two galaxies with Type II.o profiles (NGC 2273 and NGC 2950), the break occurs well *outside* what appears to be the outer ring; see Figure 8, bottom panels. In these cases, the break is apparently *not* related to the bar’s OLR. We therefore consider these to be examples of “classical truncations,” so named because they seem sim-

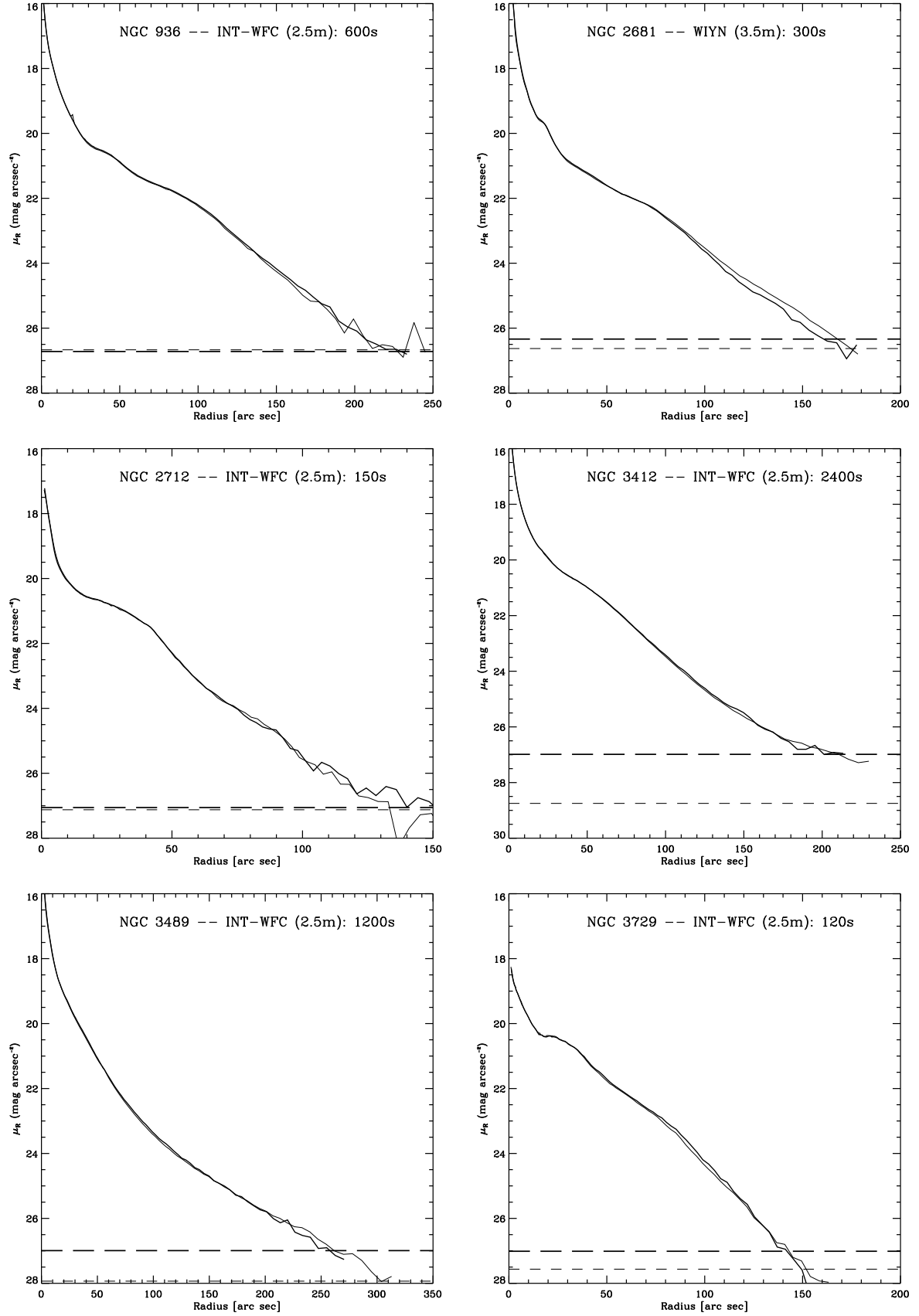


FIG. 4.— Comparison of profiles from SDSS images (thick lines) with profiles from deeper images of the same galaxy obtained with other telescopes (thin lines). The telescope and exposure time of the deeper image is indicated within each plot. The horizontal dashed lines mark the sky uncertainty limits μ_{crit} . Even though the SDSS images are short exposures, in most cases they match the profiles from deeper exposures quite well.

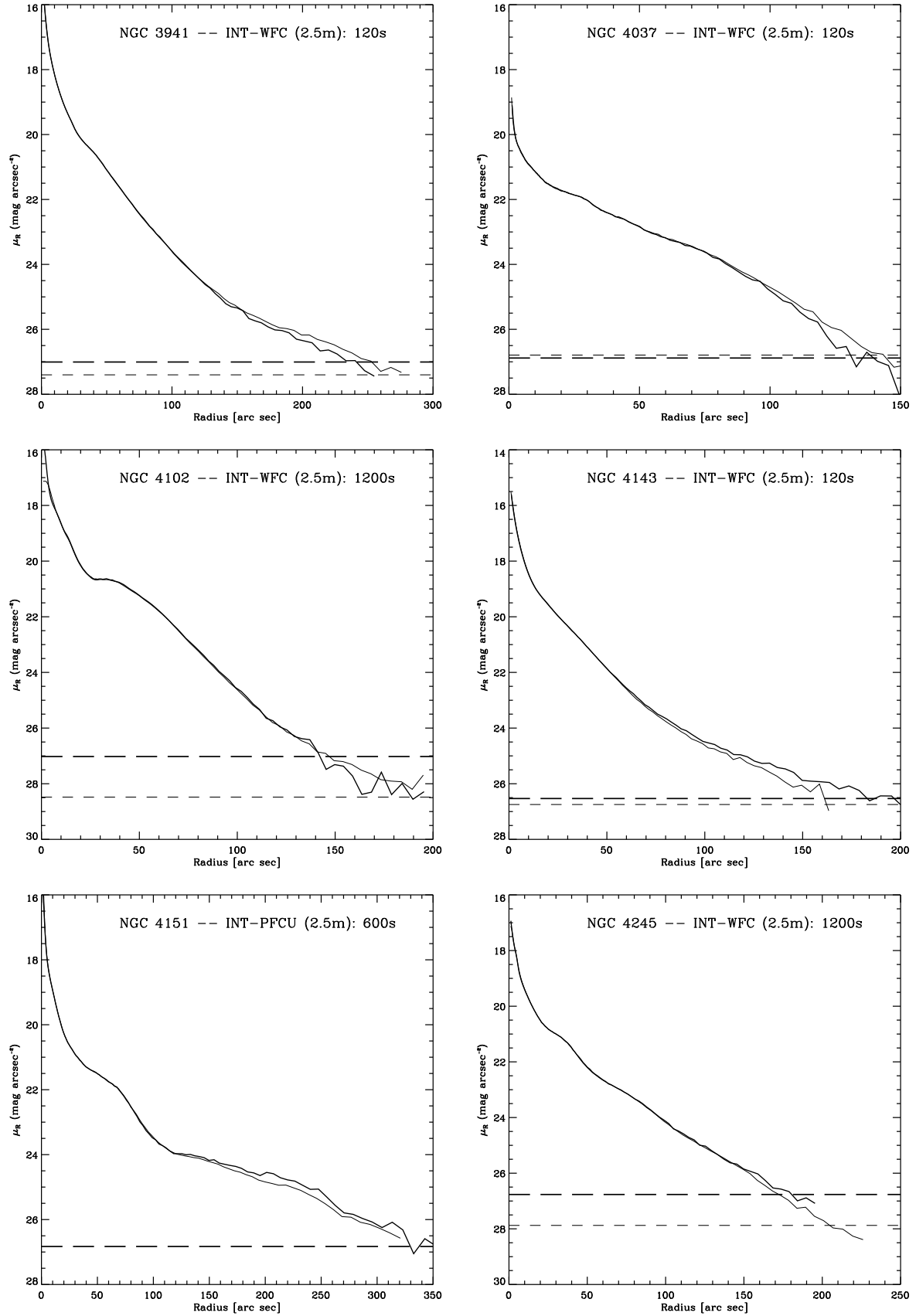


FIG. 4.— continued.

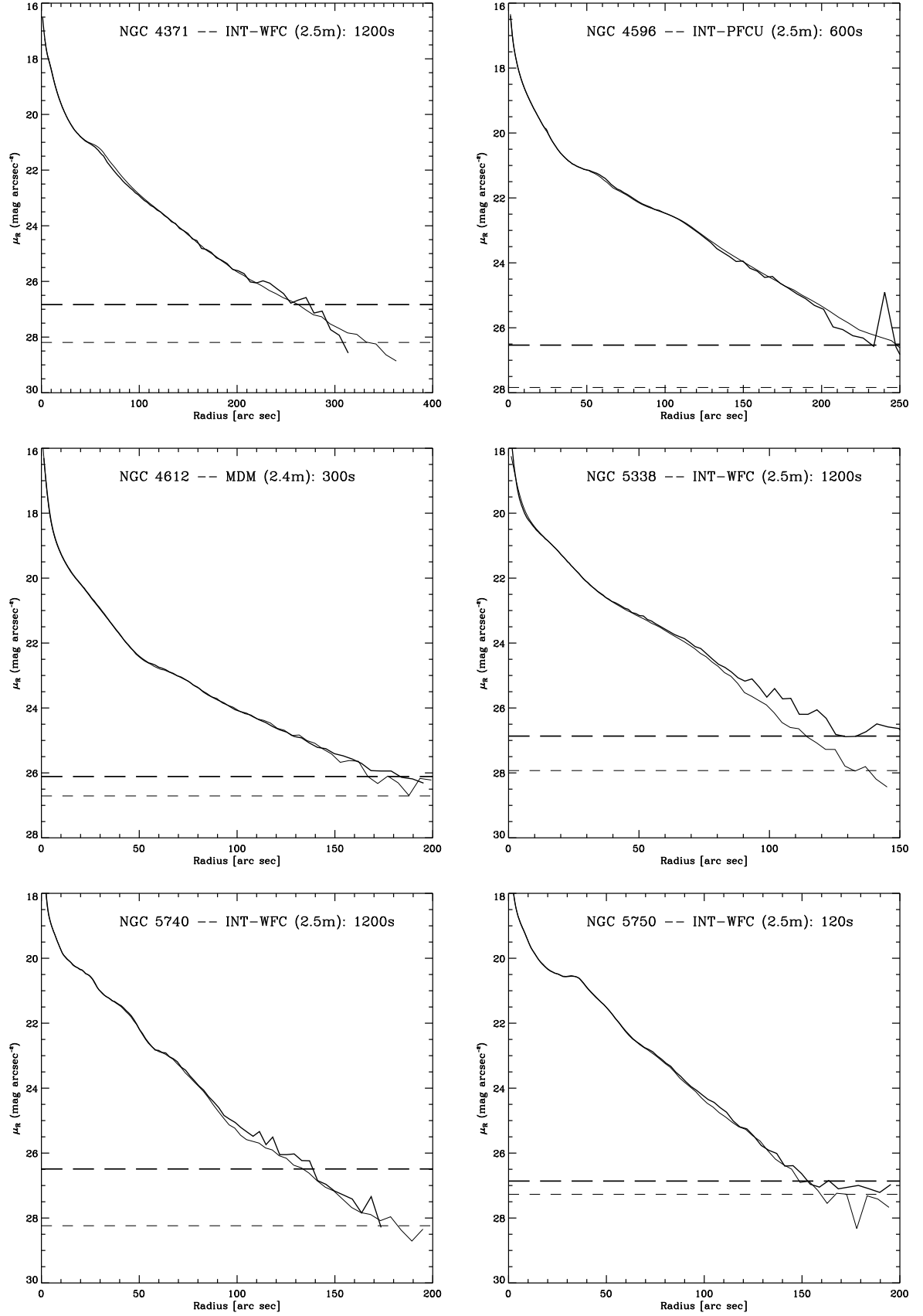


FIG. 4.— continued.

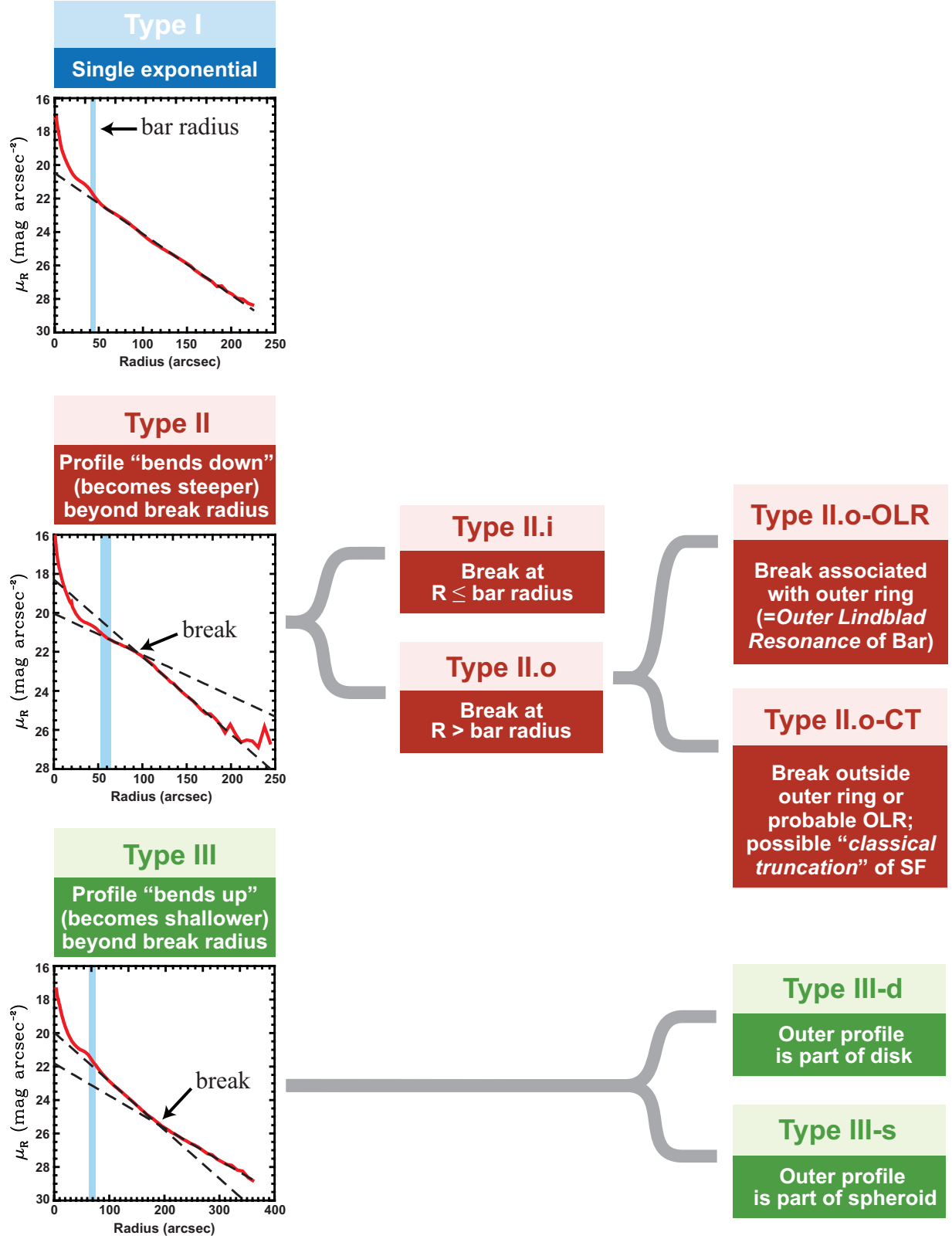


FIG. 5.— An overview of our scheme for classifying surface-brightness profiles. The basic level recognizes Types I, II, and III, based on their overall shape (ignoring the central excess associated with the bar/bulge). Type II profiles can be further subdivided into II.i and II.o, based on where the break in the profile is located. Finally, Type II.o and Type III profiles can be further classified based on the probable nature of the break (Type II.o-OLR vs. Type II.o-CT) or the disk vs. spheroid nature of the outer profile (Type III-d vs. Type III-s). See text and subsequent figures for more details.

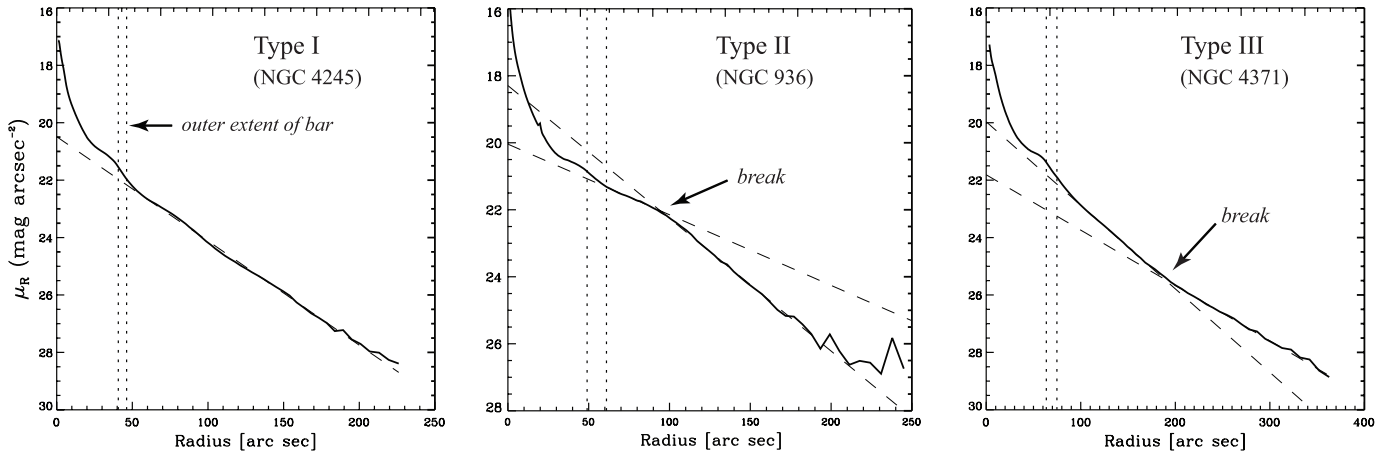


FIG. 6.— The three basic classes of surface-brightness profiles. Type I (left) is the simple, single-exponential profile; note that we focus on the profile *outside* the bar region (the vertical dotted lines mark lower- and upper-limit estimates of the bar size, from Table 1). Type II profiles (center) have a break at which the profile changes slope from shallow to steep. Type III profiles (“antitruncations,” right) have the reverse behavior: the profile slope changes from steep to shallow at the break.

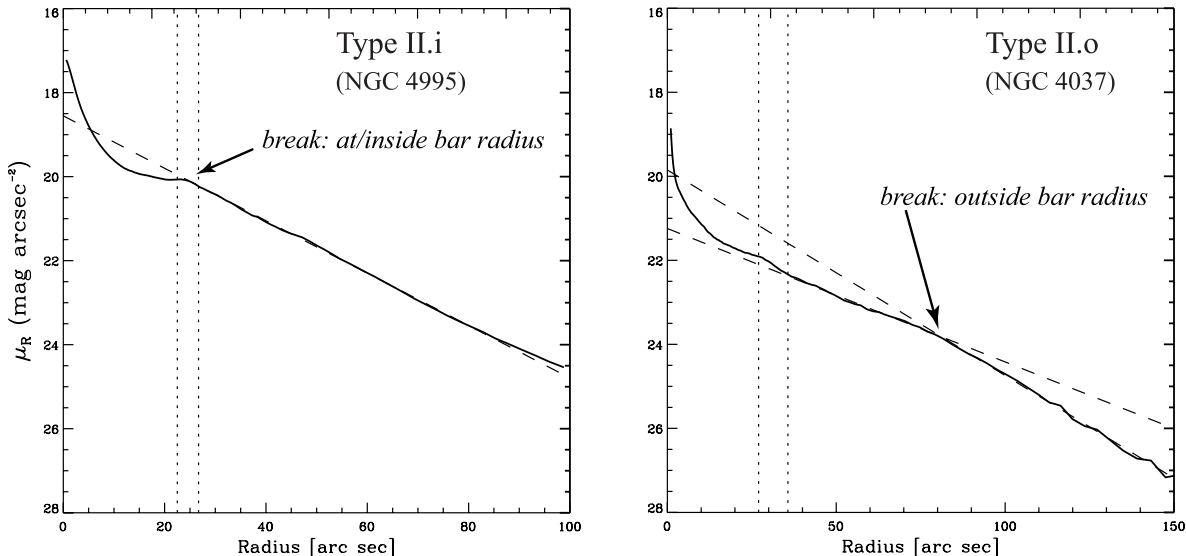


FIG. 7.— Examples of our Type II profile subdivisions. On the left is a Type II.i profile, in which the break occurs near the end of the bar (so that the deficit is fully *inside* the bar radius). On the right is a Type II.o profile, with the break occurring well *outside* the bar.

ilar to the “truncations” first seen in edge-on, late-type galaxies (e.g., Pohlen et al. 2004, and references therein). Such breaks are usually supposed to be related to star-formation thresholds (e.g., Kennicutt 1989; Schaye 2004; Elmegreen & Hunter 2006). We call these profiles **Type II.o-CT**.

In NGC 5338, the break is at 3–4 times the bar radius⁷. Although no outer ring is visible in this galaxy, we conclude that this break is outside the probable radius of the OLR, and so we classify the profile as Type II.o-CT(?). In the case of NGC 4037, the break is at 2.4–3.1 time the bar radius, and again there is no visible outer ring. Because the break is at a low surface brightness level — as is the case for the breaks in NGC 2273, 2950, and 5338 — it is tempting to consider this another classical trun-

cation. However, since the break radius is not clearly beyond the limits of plausible OLR breaks, the situation is ambiguous; we leave this galaxy with an unmodified II.o classification.

Finally, we note that we do *not* see any examples of the “Type II-AB” (“apparent/asymmetric break”) profiles that Pohlen & Trujillo (2006) found in 13% of their galaxies. They noted that these seemed to occur only in Sc–Sd galaxies and not in any of the earlier (Sb–Sbc) galaxies in their sample; it is apparently due to strong lopsidedness in the outer isophotes. Since all galaxies discussed in *this* paper are Sb or earlier, this would appear to reinforce their suggestion that the Type II-AB profile is a late-type phenomenon.

⁷ Depending on which of the two bar-radius measurements one uses.

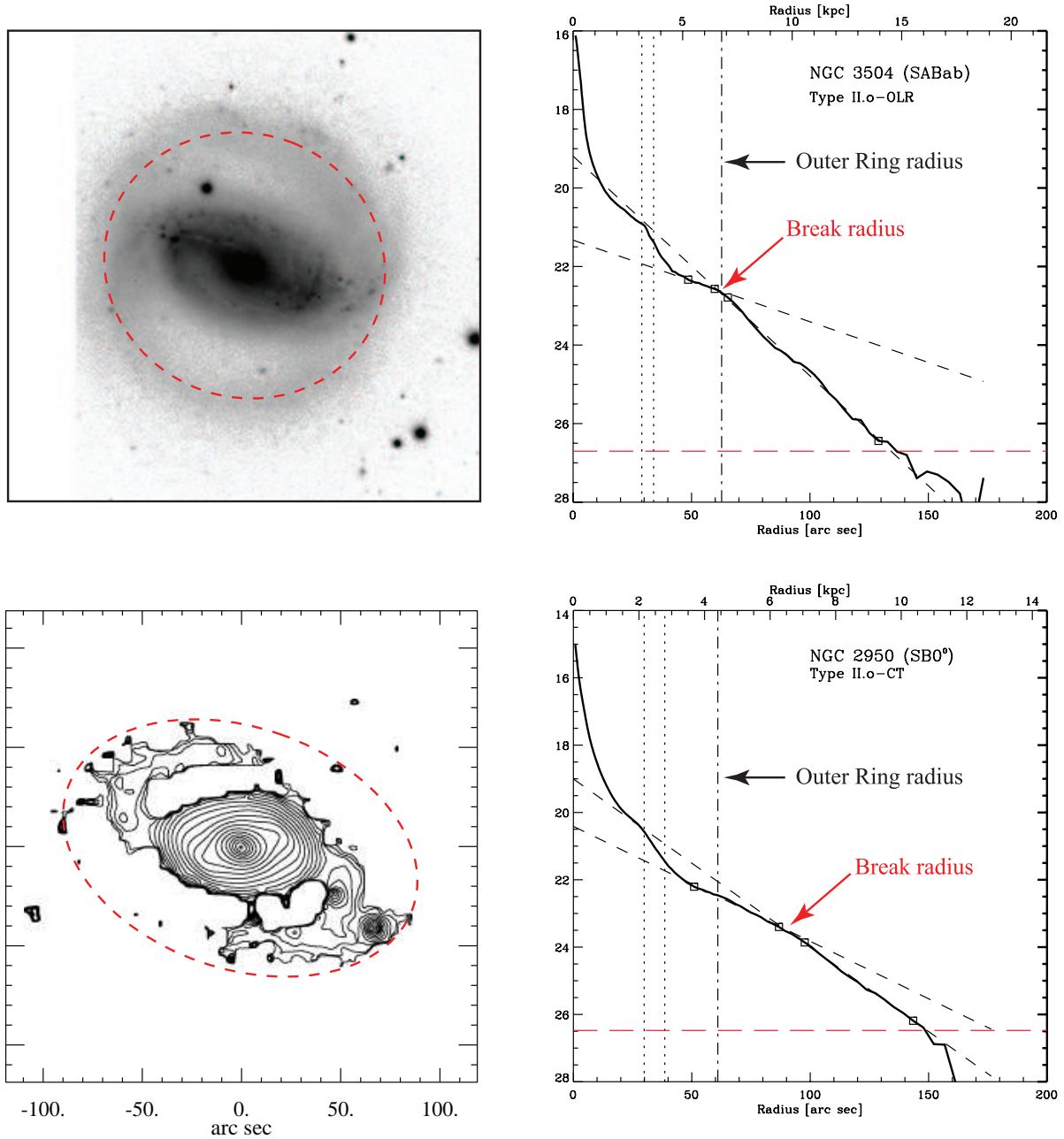


FIG. 8.— Comparison of Type II.o-OLR and Type II.o-CT profiles. NGC 3504 (top panels) has a Type II.o profile where the break coincides with an outer ring; NGC 2950 (bottom panels) has a Type II.o profile where the break is well *outside* the outer ring. In both figures, the break radius is indicated by the dashed red ellipse (left-hand panels) and the red arrow (right-hand panels). For NGC 3504, we display the SDSS *r*-band image; for NGC 2950, we have subtracted a model of the outer disk from the SDSS image in order to bring out the (faint) outer pseudo-ring.

We also define an interpretive subdivision for Type III profiles. This is based on whether the evidence indicates that the outer part of the profile, beyond the break, is still part of the disk (**Type III-d**) or whether it is due to a more spheroidal component (**Type III-s**). The distinction between these two subdivisions is explained in somewhat more detail, with illustrative examples, in Erwin et al. (2005).

The clearest signature of a spheroidal component (Type III-s) is when the isophotes for an inclined galaxy become progressively rounder at larger radii, and the

transition between inner and outer slopes is smooth, not abrupt (Figure 9). This is what one would expect if the light at large radii is coming from a rounder structure, in which the inclined disk is embedded.

Cases where the outer light is part of the disk (Type III-d) can be identified in two ways. When the galaxy is inclined, the outer light appears to have the same ellipticity as the inner light, suggesting it is still coming from the disk (Figure 10). In other cases (e.g., face-on galaxies, where both disks and spheroids will produce roughly circular isophotes), we can sometimes see clear

spiral arms in the outer region, which again are signs that the outer light is still coming from a disk (Figure 11).

One could argue that the Type III-s classification doesn't really represent the *disk* profile, so that we might just as easily refer to these as, e.g., "Type I + spheroid" and reserve "Type III" strictly for the disk cases (what we currently call Type III-d). For consistency, however, and because in some cases we cannot be certain the outer light *is* from a spheroid, we keep the Type III-s term.

4.4. Profiles with Multiple Classifications

The Type I/II/III classification scheme, with the associated subtypes, does a good job of capturing the main variations we see in the disk profiles. Nevertheless, nature is nothing if not perverse, and there are at least four galaxies whose profiles are more complicated, combining elements of more than one type. (Pohlen & Trujillo 2006 also found examples of composite profiles in their late-type sample.) These are all cases where the inner part of the profile (that is, outside the central photometric "bulge" and any excess or "shoulder" associated with the bar) has a Type II character, but at larger radii the profile appears to be Type III; see Figure 12 for two examples. We do *not* see any profiles with *two* downward-bending breaks, nor do we see any cases of Type III profiles with truncations.⁸

In some galaxies (e.g., NGC 3412, Figure 9), the complex profile appears to be a simple case of a Type II *disk* plus light from a spheroid which dominates at large radii to produce the Type III-s profile. There are other galaxies where the outer excess light is still part of the disk. For example, the outer excess light in the profile of NGC 3982 ($r > 53''$) comes from a region dominated by two blue spiral arms (Figure 11). In all cases, we indicate such composite profiles with a plus sign, e.g., "Type II.o-OLR + III-d," where the first type is the innermost.

There are also some profiles where we have hints of excess light at large radii (e.g., NGC 3507), but the S/N at those radii is too low for us to be absolutely certain. To deal with these cases, we use a criterion based on the magnitude difference between the point where the apparent outer excess begins ($\mu_R = 25.5$ in the case of NGC 3507) and the limiting magnitude from the sky-background uncertainty ($\mu_{\text{crit}} = 26.6$ for NGC 3507). If this difference is > 1.5 mag, we consider the Type III classification secure and list it in Table 4; if it is between 0.5 and 1.5 mag, we include a tentative note on the plot (" [+ III?]" in the case of NGC 3507) and in the "Notes" column of Table 4; if the difference is smaller than 0.5 mag (e.g., NGC 3368 or NGC 4267), then we do not consider it a significant detection.

4.5. Exponential Fits and Measuring the Break Radius

We fit exponentials to portions of the surface-brightness profile which appear approximately linear on the plots. In almost all cases, we look for a reasonably linear zone outside the bar region; in many galaxies, the bar is marked by an excess "shoulder" over the exponential profile outside (see, e.g., NGC 4245 and 936 in Fig. 6). We also exclude clear, extended bumps due to outer rings, on the principle that such features can be

treated as excess flux on top of an underlying exponential. When fitting regions of the profile that extend down to our limiting surface-brightness level μ_{crit} , we set the outer limit of the fit at the radius where $\mu(r) = \mu_{\text{crit}}$, except in cases where the profile becomes visibly noisy near that limit, in which case we stop the fit just outside the beginning of the noisy part of the profile.

After isolating the region or regions to fit, we regrid the data to a linear radial spacing using cubic-spline interpolation, and then perform a simple linear, least-squares fit. We regrid because the logarithmic spacing in the original profile means more data points at smaller radii; this can bias the fit so that it does not match the outer part of the profile well. This is not an ideal solution, by any means; in doing this, we ignore the fact that the data points at smaller radii have higher S/N, and could provide better constraint on the fit if they were properly weighted — at least if the underlying profile were known to be intrinsically exponential. However, local non-exponentiality (e.g., due to spiral arms or dust) at small radii could then bias the fit. We note that a limited comparison was made by Erwin (2005), who found that exponential slopes for Type I profiles obtained this way generally agreed with slopes determined by Baggett, Baggett, & Anderson (1998) for the same galaxies, even though the latter authors used Poisson-noise weighting in their fitting.

For the case of Type II.o profiles, we attempt to fit the parts of the profile both inside and outside of the break in a piecewise fashion, as done by, e.g., Pohlen et al. (2002) and Pohlen & Trujillo (2006). Pohlen et al. demonstrated that it makes sense to try doing this even when one is dealing with classical truncations in late-type spirals, since the profile outside the break is clearly exponential. One might, however, ask why we bother fitting two exponentials to some of the more extreme Type II.o profiles, where the inner profile is "exponential" only over a relatively short range (e.g., NGC 2962 and NGC 3945; see also the discussion of NGC 6654 ("VII Zw 793") in Kormendy 1977). We do this because we want to start from a position of agnosticism on the question of when a profile is "truncated" or not. Discussions of disk truncation usually assume that "the" exponential disk is the part of the profile *inside* of the break. In contrast, the traditional picture of Type II profiles is that the exponential disk is the *outer* part of the profile, outside of the break — even if the inner profile is also exponential. If we resolutely fit *both* parts of the profile, inside and outside the break radius, we can use the results as part of a general analysis of Type II.o profiles (Erwin et al. 2007). In addition, there are a small number of Type II.o profiles which are genuinely ambiguous: the break is located at about the right radius for an OLR, but the inner profile is fairly steep and extended and so the break is *also* plausible as a classical truncation. Future analysis — and better development of models which predict the characteristics of broken profiles — may allow us to more cleanly classify such profiles, but in the meantime we adopt a pluralistic approach. We note that there are only two Type II.o profiles where the profile inside the break (i.e., between the bar and the break) is clearly non-exponential: NGC 2859 and NGC 3982⁹; for these

⁸ Pohlen & Trujillo (2006) did, however, find one case of an apparent double-downward-break profile; see their Fig. 5.

⁹ In the case of NGC 3982, we are referring to the Type II.o

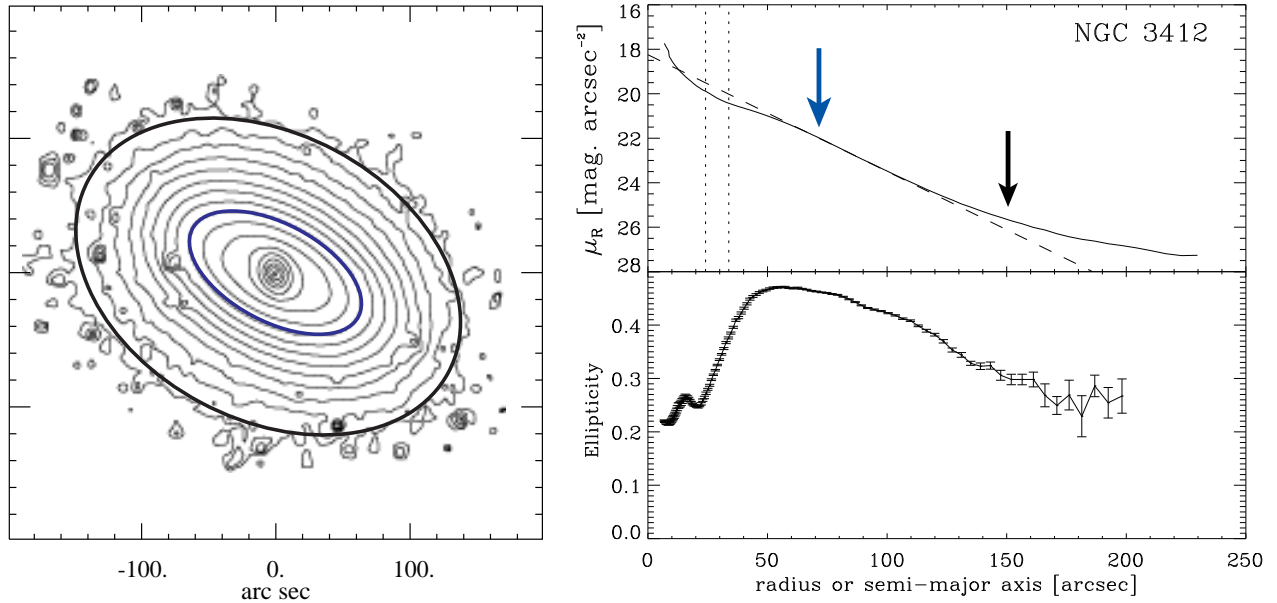


FIG. 9.— Identifying a Type III-s (“Type III-spheroid”) profile in an inclined galaxy: The outer isophotes of NGC 3412 (e.g., large black ellipse in left panel, black arrow in upper-right panel) are clearly rounder than the inner isophotes (e.g., blue ellipse and arrow), and become even rounder at larger radii (see ellipse fits in lower-right panel). This suggests that the outer part of the profile ($r \gtrsim 130''$) is due to an intrinsically rounder component — presumably the outer part of this S0 galaxy’s bulge.

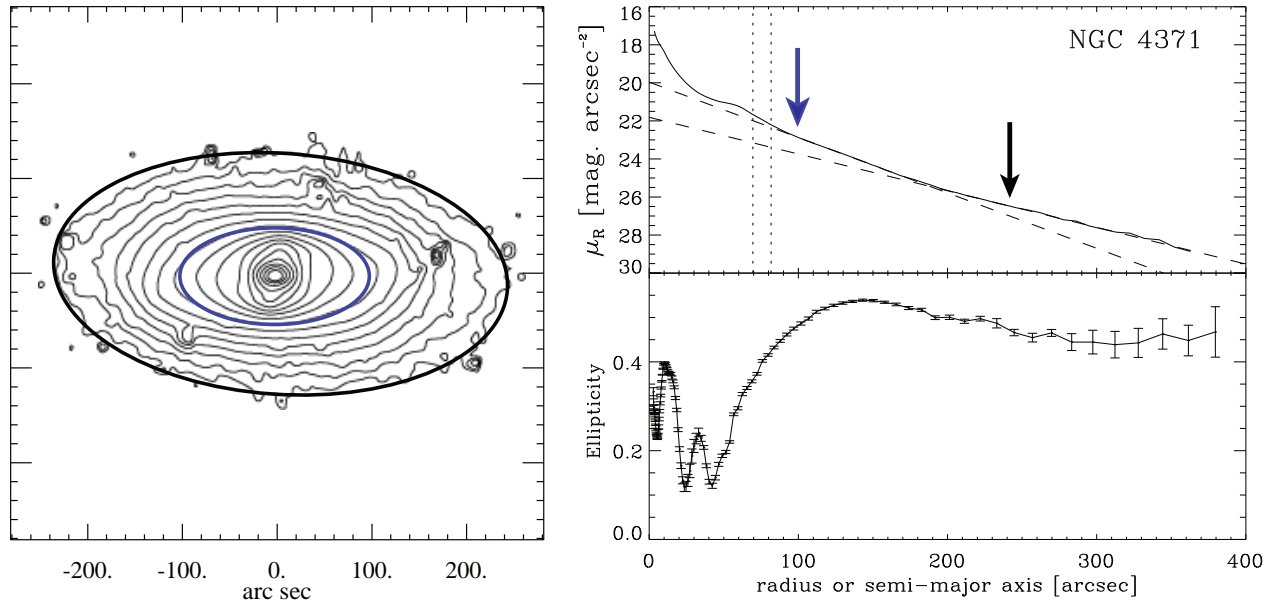


FIG. 10.— Identifying a Type III-d (“Type III-disk”) profile in an inclined galaxy: The outer isophotes of NGC 4371 (e.g., large black ellipse in left panel and black arrow in upper-right panel) are approximately as elliptical as the inner isophotes (e.g., blue ellipse and arrow) and show no signs of becoming rounder at the largest radii, suggesting that the outer part of the profile ($r > 200''$) is still part of the disk. The ellipticity peak at $r \sim 150''$ is associated with twisted and partly boxy isophotes, and is probably due to an outer ring.

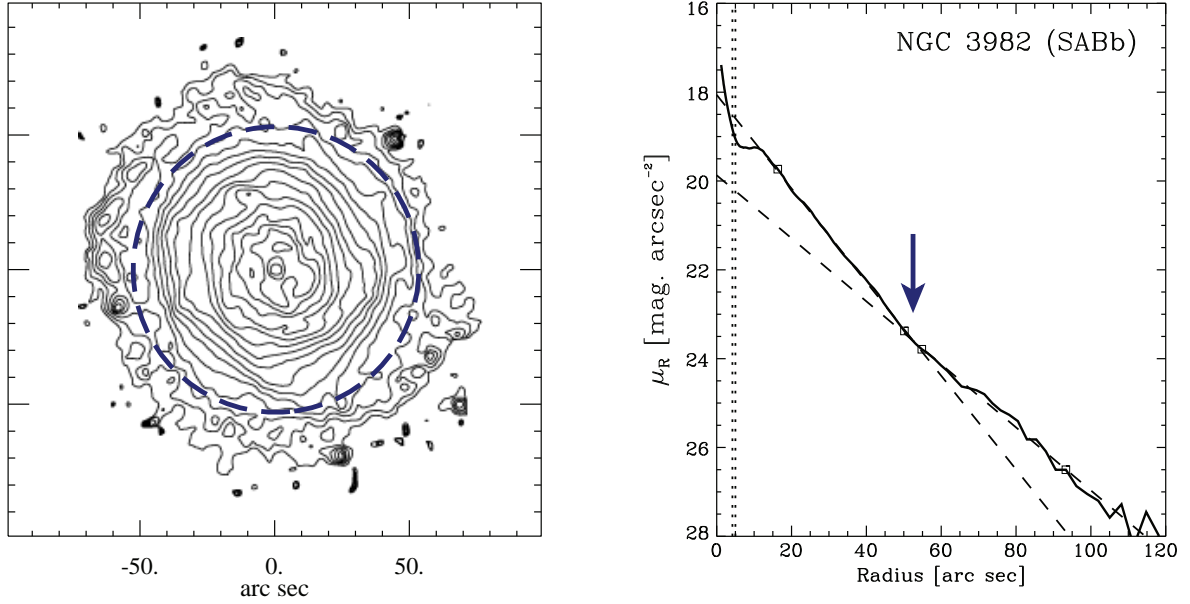


FIG. 11.— Identifying a Type III-d profile in a face-on galaxy: Although NGC 3982 is almost face-on, we can still identify the outer part of the profile ($r > 53''$) as being part of the disk because the light is clearly dominated by spiral arms. The dashed ellipse in the left panel (SDSS *g*-band isophotes) marks the break, also indicated by the arrow in the right panel (*R*-band profile).

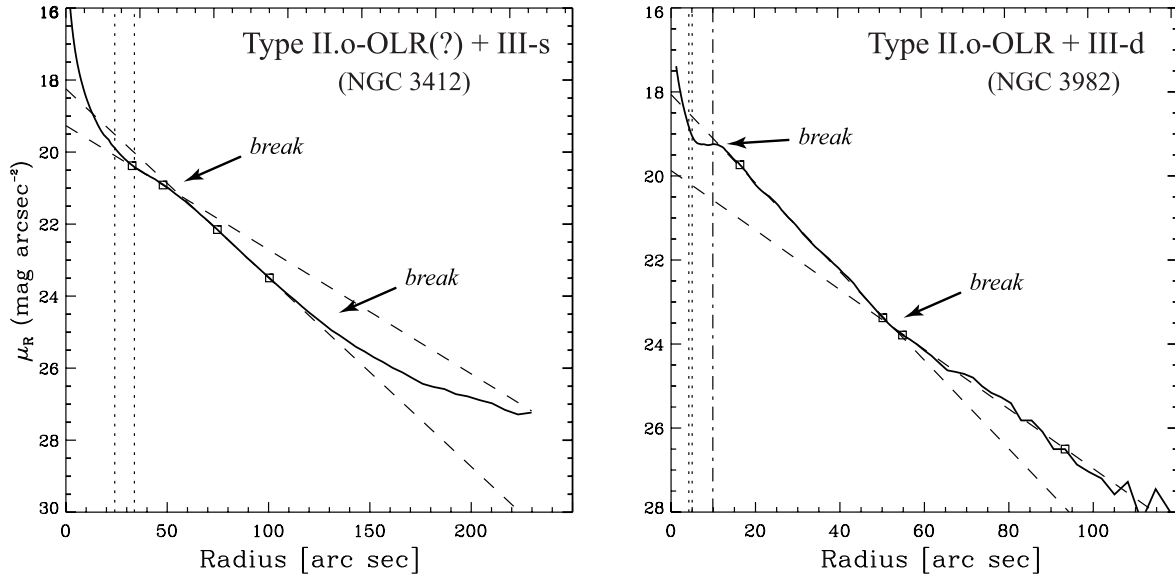


FIG. 12.— Examples of composite profiles. In both galaxies, the inner profile is Type II.o, with the break at $\sim 2 \times$ the bar radius; further outside is a second break, with a shallower profile beyond. The outermost part of NGC 3412's profile (left) corresponds to rounder isophotes (see Fig. 9); this plus the smooth nature of the outer break suggests additional light from a spheroid. In contrast, the outer break in NGC 3982's profile (right) is quite sharp, and the light beyond that point is still part of the disk (Fig 11).

galaxies, we do not report an inner scale length.

Note that we do *not* fit the outer part of a Type III profile if we can identify it as Type III-s, since in such cases the outer part of the profile is often non-exponential (e.g., NGC 3941), and in any case we are assuming that it is part of a surrounding spheroid, not an exponential subsection of the disk.¹⁰ We also do not fit the region inside the break of Type II.i profiles, since this is within the bar region and is often non-exponential. In this sense, we treat Type II.i profiles as being similar to Type I profiles: they have a single exponential disk outside the bar.

The results of these fits — the central surface brightness and exponential scale length for each of the exponential fits — are given in Table 4. The inner-profile fits (or the single fit for a Type I profile) are denoted by $\mu_{0,i}$ and h_i for the central surface brightness and the exponential scale length, respectively; the outer-profile fits are denoted by $\mu_{0,o}$ and h_o . These are *observed* values; we have not applied any corrections for inclination or dust extinction (intrinsic or Galactic). We also do not apply any redshift corrections, but since these galaxies are all at redshifts of 2000 km s^{-1} or less, any such corrections would be negligible. The measurements of the break radius and the surface brightness of the break for Type II and III profiles, also listed in Table 4, is explained below.

4.5.1. Determining the Break Radius

The break radius in Type II.o and Type III-d profiles can be estimated by eye from the profiles, or by determining the point where the exponentials fitted to the inner and outer slopes (“piecewise” fits) intersect. A somewhat more precise and rigorous approach is to fit the whole profile (excluding the bulge and bar region) with a function containing a parameterized break. We do this using a “broken-exponential” function, inspired in part by the broken power-law function known as the “Nuker law” (Lauer et al. 1995; Byun et al. 1996) used to model HST profiles of galaxy centers. Our broken-exponential function is described in more detail in Erwin (2007b), but in brief it consists of two exponential pieces joined by a transition region of variable “sharpness”:

$$I(r) = S I_0 e^{\frac{r}{\gamma}} [1 + e^{\alpha(r - R_b)}]^{\frac{1}{\alpha}(\frac{1}{\gamma} - \frac{1}{\beta})}, \quad (5)$$

where I_0 is the central intensity of the inner exponential, γ and β are the inner and outer exponential scale lengths (corresponding to h_i and h_o in our piecewise fits), R_b is the break radius, and α parameterizes the sharpness of the break. Low values of α mean very smooth, gradual breaks, while high values correspond to abrupt transitions; typical values of α for our profiles range between 0.1 and 1. S is a scaling factor, given by

$$S = (1 + e^{-\alpha R_b})^{\frac{1}{\alpha}(\frac{1}{\gamma} - \frac{1}{\beta})}. \quad (6)$$

The inner and outer scale lengths from the broken-exponential fits generally agree quite well with the piecewise fits: the median difference is 1–5%, depending on whether one compares inner or outer scale lengths, and whether one is considering Type II.o or Type III profiles.

¹⁰ We do list approximate “break radii” for such profiles in Table 4; these are the radii where the outer profiles begin to dominate over the inner exponentials.

An example of a broken-exponential fit to one of our profiles is shown in Figure 13. The only profiles for which we do not use this approach are those for which the inner region is non-exponential — specifically, the Type II.o profiles of NGC 2859 and NGC 3982, where the break radius and surface brightness is measured by eye.

For Type I and Type II.i profiles, we provide *lower limits* on potential break radii in Table 4, based on where the profile reaches μ_{crit} . This is indicated by the “>” symbols in Table 4. Since the Type II.i profiles *do* have breaks at much smaller radii (i.e., near the end of the bar), we list these break radii separately in Table 5. Break radii for Type III-s profiles are listed in Table 4; these are approximate values measured by eye, and indicate the radius where the outer excess light (presumed to come from a spheroid rather than the disk) begins to deviate from the inner exponential.

5. PROFILES AND NOTES FOR INDIVIDUAL GALAXIES

Figure 14 presents the individual surface-brightness profiles for all the galaxies in our sample. For each galaxy, we plot the azimuthally averaged surface brightness profile from our fixed-ellipse fits, exponential fits to different regions of each profile, bar sizes (a_ϵ and L_{bar} , from Table 1), and sizes of outer rings, if any (see Table 1). We do not apply any extinction corrections, intrinsic or Galactic, to these profiles.

5.1. Note on Individual Galaxies

Here, we include notes for individual galaxies. If a galaxy is *not* listed here, then the reader is directed to Erwin & Sparke (2003) and Erwin (2005) for explanations of how the bar sizes and disk orientations were determined. For the reader’s convenience, we include the profile type immediately after the galaxy’s name.

NGC 718 (II.o-OLR). See Erwin & Sparke (2003). The break in the profile at $\sim 41''$ matches the outer pseudoring (studied by Kennicutt & Edgar 1986). Note that there is an additional, faint ring at larger radii, visible as a bump in the profile at $r \sim 70''$. The scale length ($24''$) of the major-axis fit by Baggett, Baggett, & Anderson (1998) is intermediate between our h_i and h_o values; this is not surprising, since their fit extends somewhat beyond the break radius and thus includes light from both parts of the profile.

NGC 936 (II.o-OLR(?)). See Erwin & Sparke (2003). This is one of the stronger cases of a probable OLR system: there is no visible outer ring in this S0 galaxy, but the break is at about twice the bar radius. The Type II (broken-exponential) nature of the profile is not always visible in shallower exposures (e.g., Kent & Glaudell 1989; Laurikainen et al. 2005), but has previously been noted by Kormendy (1984) and Wozniak & Pierce (1991). Baggett, Baggett, & Anderson (1998) fit their major-axis profile using a disk with a large hole, another indication of a Type II profile; their disk scale length ($23.8''$) is a reasonably good match to our $h_o = 27.4''$. The break – and the relatively shallow inner slope – also agree with the “outer lens” classification by Kormendy (1979).

NGC 1022 (I). See Erwin & Sparke (2003). Note that the outer ring is associated with a slight excess in the profile at $r \sim 50\text{--}60''$; the profile decreases beyond this point, but recovers to an exponential for $r \gtrsim 100''$.

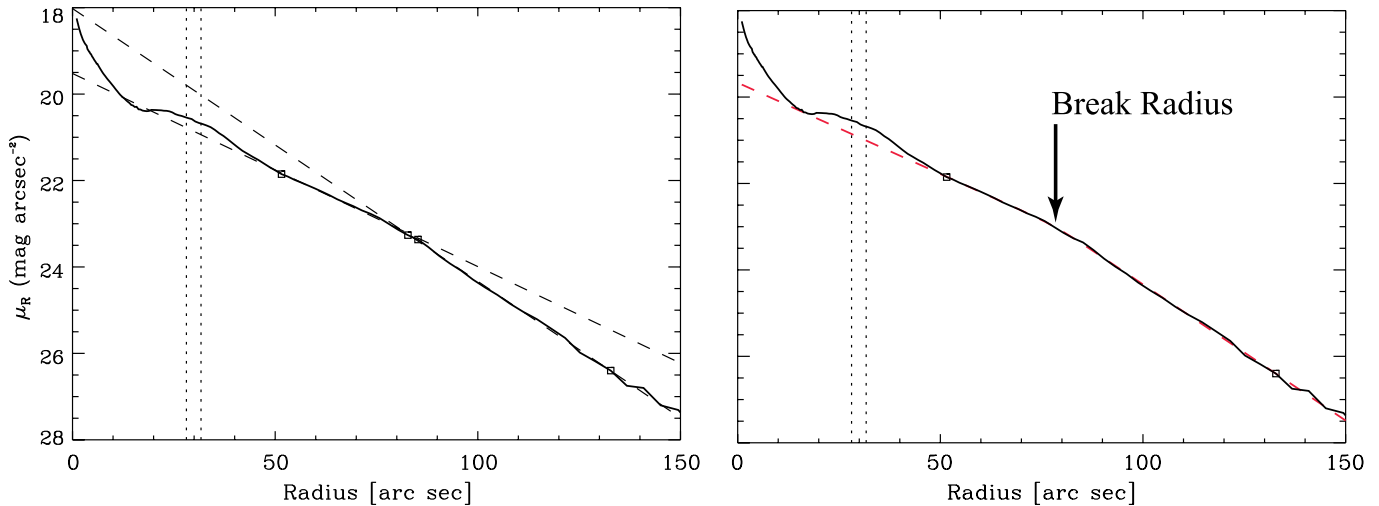


FIG. 13.— Example of a broken-exponential fit to the Type II.o profile of NGC 3729. *Left*: Piecewise fit to zones (delimited by small squares) inside and outside apparent break. *Right*: Broken-exponential fit (dashed red line) to the same profile; small squares mark the inner and outer limits of the fitted region. The break radius of the fit is $R_b = 78.5''$.

This is one of the few galaxies in our sample for which we could find no R -band photometric calibration.

NGC 2273 (II.o-CT). See Erwin & Sparke (2003). This galaxy is notable for having *two* distinct outer rings (as well as an inner pseudoring just outside the bar and a nuclear ring inside the bar); both outer rings are associated with H I (van Driel & Buta 1991). As discussed in Erwin et al. (2007), we identify the smaller of the two outer rings with the bar’s OLR, so the break in the profile (just beyond the outermost ring) is then judged to be a classical truncation.

NGC 2681 (I). See Erwin & Sparke (1999) and Erwin & Sparke (2003). Even though we treat the “outer disk” as the region outside the largest of this galaxy’s three bars ($r \gtrsim 110''$), the exponential fit to the outer disk matches the disk at $r \sim 30$ – $50''$ (outside the middle bar) as well.

NGC 2712 (I). See Erwin (2005) for notes on the bar measurements; the disk orientation is from the H I map of Krumm & Shane (1982). There is a small bump in the profile associated with the outer ring, whose existence and size we report here for the first time; there is also a very extended excess associated with spiral arms outside the bar ($r \sim 30$ – $60''$). Note that in principle it might be possible to interpret this excess as a Type II.o-OLR profile outside the bar, with the exponential at $r > 50''$ making the whole profile Type II.o-OLR + III like that of NGC 3982.

NGC 2787 (I). See Erwin & Sparke (2003) and Erwin et al. (2003). Scattered light problems prevent tracing the disk to fainter light levels, and make it difficult to be certain about the possible excess light at $r \gtrsim 130''$. (Similar problems are present in images taken with the Jacobus Kapteyn Telescope in 2001 January 29, obtained from the ING Archive, which we used for the photometric calibration.)

NGC 2859 (II.o-OLR). See Erwin & Sparke (2003). This is one of three galaxies with “extreme outer-ring” profiles; the profile between the end of the bar and the outer ring is in this case clearly *not* exponential, and so we do not attempt to fit it. The disk orientation param-

eters presented here are updated slightly from those in Erwin & Sparke (2003) and Erwin (2005), and are based on the SDSS image. Laurikainen et al. (2005) suggest a somewhat higher inclination (outer-disk ellipticity = 0.24 instead of 0.13) than we use, based on their deep B -band image; however, the profile derived using their orientation parameters is very similar to the profile we present here.

NGC 2880 (III-s). See Erwin & Sparke (2003). This is the most dramatic case of a Type III-s profile, with most of the light probably coming from a spheroidal component; an E/S0 classification might be more appropriate for this galaxy. The central surface brightness of our exponential disk fit is undoubtedly an overestimate, since it neglects any contribution from the spheroid.

NGC 2950 (II.o-CT). See Erwin & Sparke (2003). There is a faint outer ring (e.g., Sandage 1961) associated with a very slight excess in the profile at $r \sim 60''$. The break in the profile is well outside this ring, making this a classical truncation (II.o-CT) rather than an OLR break (see Figure 8).

NGC 3049 (II.o-OLR(?)). This profile is slightly ambiguous, since the break is fairly close to the end of the bar, and the profile between the end of the bar and the break suggests a steeper profile (with another break inside). This is the only profile for which we include a region *inside* the bar radius in the fit. There is a slight hint of excess light at $r > 90''$, hence we include “[+III?]” in the label on the plot.

The bar size measurements have been slightly updated from those published in Erwin (2005), using a Spitzer $3.5\mu\text{m}$ (IRAC1) image from the Spitzer Infrared Nearby Galaxy Survey (Kennicutt et al. 2003).

NGC 3412 (II.o-OLR(?) + III-s). See Erwin & Sparke (2003). As shown in Erwin et al. (2005) and Figure 9, this is a clear case of an outer spheroid dominating the light at large radii; at smaller radii, the profile is Type II.o-OLR(?).

NGC 3485 (I). An alternate interpretation of the profile might be Type II.i + III; however, the part of the profile from the end of the bar out to $r \sim 50''$ is perhaps

more easily understood as an extended bar “shoulder” (as for, e.g., NGC 2712 or NGC 3507).

NGC 3489 (III-d). See Erwin & Sparke (2003). This is a somewhat peculiar Type III profile: the break is very smooth and gradual, which suggests that the outer light could be from an additive, additional component (like a bulge or halo); but the isophotes at $r > 150''$ are more elliptical than any part of the galaxy except the outer ring; see Figure 21 of Erwin & Sparke.

NGC 3945 (II.o-OLR). See Erwin & Sparke (1999) and Erwin & Sparke (2003). This is another galaxy with a very strong outer ring, similar to NGC 2859 and NGC 5701, though the break is relatively sharp.

NGC 3982 (II.o-OLR + III-d). This is perhaps the most complicated profile in our sample. The profile out to $r \sim 50''$ is a good example of the II.o form, with a ring right at the break. This is one of three galaxies with “extreme outer-ring” profiles; in this case, the profile between the end of the bar and the outer ring is *not* exponential. (Due to the small size of this ring, de Vaucouleurs & de Vaucouleurs (1964) described it as an “inner ring;” but since it lies at almost exactly twice the bar radius, it is far more likely to be an OLR-associated outer ring.) Beyond $50''$, the profile changes to a shallower exponential, forming a Type III profile. Although the galaxy is face-on, making determination of the outer geometry difficult, there is a clear pair of spiral arms at $r > 50''$, indicating that the outermost light is still from the disk (Figure 11).

Pohlen & Trujillo (2006) note the inner break associated with the ring but exclude it from their analysis; consequently, they consider this a Type III profile only. Our analysis of the Type III part of the profile matches extremely well with theirs; the inner scale length and break radius measurements agree to within 2%, and the outer scale length measurements (more affected by sky subtraction errors) differ by only 6%.

We adopt the Cepheid-based distance estimate of Riess et al. (2005), which is based on a re-analysis of the data and estimates of Saha et al. (2001) and Stetson & Gibson (2001).

NGC 4037 (II.o). This galaxy is unusually low surface brightness for our sample, with a central surface brightness of $\mu_R > 18$ mag arcsec $^{-2}$. It is also somewhat unusual in having a break well outside the bar radius: $R_{\text{brk}} = 3.1 a_e$ and $2.4 L_{\text{bar}}$. As pointed out in Section 4.3.1, this is large enough to be potentially unrelated to the bar’s OLR, but not convincingly so; we leave it with a bare Type II.o classification.

NGC 4102 (II.o-OLR + III-s(?)). Our classification of the profile is identical to that of Pohlen & Trujillo (2006), except that our deeper INT-WFC image allows us to examine the shape of the isophotes outside the second break radius better. Since these show some sign of becoming rounder at larger radii, as might be expected from a spheroid rather than an extension of the (inclined) disk, we tentatively classify the it as III-s(?), and do not attempt to fit an exponential to the outermost part of the profile.

We do, however, differ from Pohlen & Trujillo in our analysis of the Type II.o part of the profile. We fit the short, nearly flat region from $r \approx 27\text{--}35''$, which as it happens is the region just inside the radius of the outer ring; Pohlen & Trujillo fit a steeper region *outside* the

outer ring (which we consider part of the transition region). Consequently, we have rather different values for h_i and the break radius. Since our break radius is based on fitting a larger range of the profile, on both sides of the outer ring, and since the resulting break radius ($42.9''$) is closer to the radius of the outer ring ($36''$), we consider our analysis more correct.

This is one of our deepest profiles, with $\mu_{\text{crit}} \approx 28.5$ R -mag arcsec $^{-2}$. The apparent turnover at $r < 5''$ is due to saturation of the galaxy center in the INT-WFC images.

NGC 4151 (I). The best R -band image available is not large enough to guarantee good sky subtraction, so we truncate our profile at a level well above the nominal uncertainty (as determined from the corners of the image). The resulting profile agrees very well with the profile from an SDSS image (Fig. 4); unfortunately, the faintness of the outer disk means we cannot use the SDSS image to probe any further out in radius. The outer ring size is measured directly from the image, since the value from de Vaucouleurs & de Vaucouleurs (1964) appears to be an underestimate.

Laurikainen et al. (2004) reported a disk scale length of $27.1''$ from a 2D decomposition of a B -band image from the Ohio State University Bright Spiral Galaxy Survey. This is about one-third the value we find ($78.6''$; we find a very similar scale length using the SDSS r -band image).

NGC 4203 (II.o-OLR(?) + III-s(?)). This is a clear Type II.o profile with a weak but significant excess over the outer exponential at $r \gtrsim 140''$. The galaxy is close to face-on, which makes determining the shape of the outer isophotes difficult. However, there is evidence that the isophotes become systematically rounder for $r > 100''$, so our tentative conclusion is that the outer light may be coming from a spheroid.

The nature of the inner (Type II.o) break is also somewhat ambiguous, since the bar size is uncertain; as noted by Erwin & Sparke (2003) and Erwin (2005), the large value of $L_{\text{bar}} = 46''$ is almost certainly an overestimate of the bar size. So it is difficult to judge whether the break is too far out from the bar to be associated with its OLR. Nonetheless, the high surface brightness of the break suggests it is *not* due to a (star-formation-related) classical truncation (see Erwin et al. 2007), so we tentatively classify it as an OLR break.

NGC 4267 (I). For this galaxy, we adopt the distance reported by Mei et al. (2007), based on surface-brightness fluctuation measurements.

NGC 4319 (III-d). This galaxy possesses a spectacular outer 1-arm spiral, which could also be interpreted as a tidal tail. This structure produces the dramatic bump in the profile at $r \sim 70''$, obscuring the transition between the inner disk and the outer disk. The III-d classification — and the break radius measurement — is therefore somewhat dubious. A combination of bright stars and strong residual structure in the image (including flat-fielding artifacts) prevents us from reliably tracing the profile down to our nominal μ_{crit} level.

NGC 4340 (I). The outer-disk orientation parameters for this galaxy have been updated from those published in Erwin (2005); the new parameters are based on our analysis of the SDSS image from DR5. The adopted distance is the mean distance to the Virgo Cluster from Mei et al. (2007).

NGC 4371 (III-d). See Erwin & Sparke (1999) and Erwin (2005). As shown in Figure 10, the outer isophotes have roughly constant ellipticity consistent with that of the inner disk, so this is a III-d profile. For this galaxy, we adopt the distance reported by Mei et al. (2007), based on surface-brightness fluctuation measurements. This is one of our deepest profiles, with $\mu_{\text{crit}} \approx 28.2$ R -mag arcsec $^{-2}$.

NGC 4477 (I). The adopted distance is the mean Virgo Cluster distance of Mei et al. (2007).

NGC 4531 (III-s). This galaxy was *not* included in the bar-size study of Erwin (2005) because no bar was visible in the optical images. However, analysis of an H -band image from the GOLDMine database (Gavazzi et al. 2003) indicates that there *is* a bar in this galaxy. Using the same approach as Erwin (2005), we find bar sizes of $a_e = 8.5''$ and $L_{\text{bar}} = 14''$ for this galaxy, with the bar having a position angle of 127° . The distance is from Tonry et al. (2001).

NGC 4596 (I). The adopted distance is the mean Virgo Cluster distance of Mei et al. (2007). Because of the small size of the image, the outer reaches of the galaxy along the semi-major axis lie outside the image, preventing us from tracing the profile as far out as we might (even though the sky background in the far corners of the image gives a very faint μ_{crit} value).

NGC 4608 (II.i). The adopted distance is the mean Virgo Cluster distance of Mei et al. (2007).

NGC 4612 (III-d). For this galaxy, we adopt the surface-brightness-fluctuation distance reported by Mei et al. (2007).

NGC 4691 (III-d). See Erwin & Sparke (2003). The inner part of the profile ($r < 125''$) could conceivably be interpreted as a weak Type II profile, in which case this galaxy would be similar to NGC 3982.

NGC 4699 (III-d). The only R -band image we were able to obtain of this galaxy was with the NOT. Due to the small field of view and strong scattered light problems, we are not able to trace the outer disk profile out as far as we might otherwise. We note, however, that the basic Type III nature of the profile is present in a profile derived from the publically available B -band image of the Ohio State University Bright Spiral Galaxy Survey (Eskridge et al. 2002); unfortunately, the latter image also has a small field of view, and so the precise nature of the profile beyond $r \sim 150''$ remains unknown.

NGC 4995 (II.i). An extremely bright star $\sim 4'$ north of the galaxy produced a halo covering most of the central chip of the INT-WFC array; consequently, our sky subtraction in the vicinity of the galaxy is unreliable, and we stop tracing the profile at $\sim 100''$. (The sky background and uncertainty were measured in the extreme edges of the image, and do not necessarily reflect the background nearer the galaxy.)

NGC 5338 (II.o-CT(?)). See Erwin & Sparke (2003). As explained in Section 4.3.1, the break is sufficiently far outside the bar ($R_{\text{brk}} = 3.8a_e$ and $2.8L_{\text{bar}}$) that we consider an OLR connection unlikely, although no outer ring is visible. Consequently, we consider this an (uncertain) example of a classical truncation (Type II.o-CT).

NGC 5701 (II.o-OLR). See Erwin & Sparke (2003). This is one of three galaxies with “extreme outer-ring” profiles; the profile between the end of the bar and the

outer ring is only barely exponential, and the break is quite gradual. From visual inspection of the image (e.g., Erwin & Sparke 2003), it is clear that the break is due to the luminous outer ring, as for NGC 2859 and NGC 3945.

NGC 5740 (III-d). The isophotes outside the break radius show signatures of lopsided, asymmetric spirals, and the overall ellipticity is slightly higher than that of the isophotes inside the break radius. Thus, we consider the light beyond the break radius to be part of the disk, and classify this as a Type III-d profile. This is one of our deepest profiles, with $\mu_{\text{crit}} \approx 28.2$ R -mag arcsec $^{-2}$.

NGC 5806 (III-d). We find evidence for irregular and asymmetric isophotes beyond the break radius in our INT-WFC image; in addition, the isophotes retain a high ellipticity out to at least $r \sim 170''$. Consequently, we consider this a III-d profile. Our classification is otherwise similar to that of Pohlen & Trujillo (2006), including very similar values for the inner scale length and the break radius.

NGC 5832 (II.i). Our values for the disk orientation, which are derived from the outer isophotes of our INT-WFC r -band image, agree well with those derived from a Fabry-Perot $H\alpha$ velocity field by Garrido et al. (2005, $\text{PA} = 45^\circ \pm 3^\circ$, $i = 54^\circ \pm 6^\circ$). This is one of our deepest profiles, with $\mu_{\text{crit}} \approx 28.3$ R -mag arcsec $^{-2}$.

NGC 5957 (II.o). This galaxy was also observed with the NOT; the resulting profile, like all of our NOT images, has significant problems with sky subtraction (Section 2.2) but clearly shows the same overall Type II.o shape as the SDSS profile.

NGC 6012 (III-d). Our images of this galaxy are strongly affected by bright stars near the galaxy, which necessitated large-scale masking. Our profile should be considered somewhat uncertain, especially when it comes to the parameters of the outer part of the Type III profile.

NGC 6654 (II.o-OLR). Our profile is very similar to that of Kormendy (1977), who commented on the extreme shallowness of the inner profile and the relatively sharp break; our deeper profile shows that the outer slope is definitely exponential.

NGC 7177 (III-d). The shape of the outer isophotes is somewhat hard to determine due to the low signal-to-noise, so our III-d classification is uncertain. The broad, smooth transition between the inner and outer exponentials is similar to that of NGC 3489.

NGC 7280 (II.o-OLR(?)). The profile is derived from our combined deep INT-WFC images, supplemented by a profile from our WIYN image at $r < 5''$, since the latter was higher resolution and was less saturated in the center. Figure 3 compares the individual profiles from both images. The composite profile is the deepest one in our sample, with $\mu_{\text{crit}} \approx 29.0$ R -mag arcsec $^{-2}$. The excess flux at $r > 100''$ in the INT-WFC profile appears to be real, but this is a region where we have heavily masked extended halos from nearby bright stars, so it is very difficult to derive accurate isophote shapes. Since the deviation from the outer exponential starts at only ~ 1 mag arcsec $^{-2}$ above μ_{crit} , we consider this a tentative III profile only.

The inner part of the profile ($r < 100''$) is clearly Type II.o. Whether this is likely an OLR break or a classical truncation is somewhat harder to determine (there is no visible outer ring to help us), because the two estimates

of the bar length vary so much. The break radius is at ~ 4.4 times a_e , but only 1.9 times L_{bar} . Since the latter value is perfectly consistent with an OLR interpretation, and since the break occurs at a high surface brightness level inconsistent with classical-truncation predictions (see Erwin et al. 2007), we tentatively classify this as an OLR break.

NGC 7743 (I). Due to the relatively small size of the WIYN image, we are unable to trace the profile of this galaxy very far out. There is a suggestion of a break, but nothing definite, so we consider this an (uncertain) Type I profile.

IC 676 (I). See Erwin & Sparke (2003). There is an extended excess on top of the underlying exponential between $r \approx 30$ and $55''$, probably due to the outer ring.

IC 1067 (II.o-OLR(?)). The outer-disk orientation parameters for this galaxy have been updated from those published in Erwin (2005), based on our analysis of the SDSS image and our INT-WFC images (the latter have higher S/N than the SDSS image, but suffer from strong scattered light from nearby bright stars).

Our classification of this galaxy as II.o-OLR(?) is essentially identical to that of Pohlen & Trujillo (2006), though they were unable to measure the inner scale length and break radius.

UGC 3685 (I). There is a suggestion of a downward break in the profile at $r \sim 195''$, but beyond this point the profile appears to recover and approach a continuation of the exponential fit, so we consider this a Type I profile.

UGC 11920 (II.o-OLR(?)). See Erwin & Sparke (2003). The profusion of foreground stars in our image of this galaxy makes it impossible to trace the profile as far out as our μ_{crit} measurement would suggest.

6. DISCUSSION AND SUMMARY

We have presented surface-brightness profiles for a sample 66 barred, S0 and early-type spiral galaxies. These profiles, derived from R -band images, have been classified into several categories based on their overall shape. Our basic classification is an extension of Freeman’s (1970) Type I and II system:

- Type I: single exponential profiles, making up 27% of the sample;
- Type II: profiles with a downward break, with a steep exponential outside the break and (usually) a shallow exponential inside, making up 48% of the sample;
- Type III (antitruncations): profiles with an upward break, with a steep exponential inside the break and a shallow exponential (or sometimes non-exponential) profile outside, making up at least 30% of the sample.

There are four galaxies (6% of the sample) which combine Type II and III characteristics — that is, they have a shallow profile beginning just outside the bar, followed by a break to a steeper profile, followed by a break to a shallower profile at the largest radii (e.g., Figure 12).

We recognize several subdivisions within these general categories. At a descriptive level, we note that a few Type II profiles have “inner” breaks, near or at the end of the bar (Type II.i), while the majority have “outer” breaks, beyond the end of the bar (Type II.o).

The Type II.i profiles are rare (only 6% of the sample). These appear similar to profiles seen in N -body simulations of bar formation (e.g., Athanassoula & Misiriotis 2002; Valenzuela & Klypin 2003), and thus we suspect they are stellar-dynamical side effects of the bar-formation process.

Type II.o profiles, on the other hand, are common (42% of the sample), and appear to fall into two subtypes. Type II.o-OLR profiles (35% of the sample) are those where the break is close to an outer ring, or to where an outer ring would be expected (2–3 times the bar radius). Since outer rings are understood as being due to the Outer Lindblad Resonance (OLR) of the bar (e.g., Buta & Combes 1996), we suggest that these breaks are associated with the OLRs as well (see Erwin et al. 2007). Profiles where the break is located well outside the outer ring (or the likely radius of the bar’s OLR, if there is no visible outer ring) are assumed to be similar to the “classical truncations” of late-type spirals and are called Type II.o-CT; these make up only 5% of the sample. (One galaxy, NGC 4037, is ambiguous and could fall into either of these subtypes.) More detailed arguments in favor of these respective classifications will be presented in Erwin et al. (2007).

We also subdivide the Type III profiles on an interpretative basis (see Erwin et al. 2005). In some cases, we can use the shape of the outer isophotes, or the presence of clear disk features such as spiral arms, to argue that the outer part of the profile is still part of the disk (Type III-d, 18% of the sample). In other cases, the morphology suggests that the outer part of the profile is actually due to light from a separate, more spheroidal component, added to that of the disk (Type III-s, 12% of the sample); these may be cases of extended bulges or luminous stellar halos.

There are four galaxies with limited evidence for Type III profiles at very large radii; these are indicated in the Notes column of Table 4. Taking these into account would raise the Type III frequency to 36%, and in principle it could be higher still, since we may be missing light at large radii in some of our shallower images.

Pohlen & Trujillo (2006), who used essentially the same classification system as presented here, studied a sample of late-type spirals (Sb–Sm). Although the sample selection was not identical, it is similar enough to make for an interesting comparison, particularly if we focus on the barred galaxies (that is, those galaxies with SB or SAB classifications from RC3) in their sample. In what follows, we will use “late types” to refer to the barred, Sbc–Sm subset of the Pohlen & Trujillo sample (47 of the 85 galaxies in their sample with disk-profile classifications).

The comparison shows some striking differences between early and late types. In particular, Type I profiles — the paradigmatic single-exponential disk profiles — are much rarer in the late types ($11 \pm 5\%$ vs. $27 \pm 5\%$), while Type II profiles are significantly *more* common in the late types ($77 \pm 6\%$ vs. $48 \pm 6\%$). Type III profiles are slightly rarer in the late types, but not significantly so ($23 \pm 6\%$ vs. $30 \pm 6\%$). When we look at subclasses, other differences appear. By far the most common subclass of Type II.o profiles in the early types are the OLR breaks (Type II.o-OLR), which makes up $35 \pm 6\%$ of our sample. But in the late types, OLR breaks are only $11 \pm 5\%$ of the

sample, while classical truncations (found in only $5 \pm 3\%$ of the early types) are found in almost half ($45 \pm 7\%$) of the late types; late types also have apparent/asymmetric breaks (Type II-AB, $19 \pm 6\%$ of the sample), which we do not find in the early types. Curiously, Type II.i profiles seem to be equally rare in both early and late types ($6 \pm 3\%$ and $4 \pm 3\%$, respectively).

A similar analysis of the corresponding *unbarred* S0 and early-type spirals will be presented and discussed in a subsequent paper (Gutiérrez et al. 2007). Other papers will examine the nature of the Type II and III profiles, their connection to bar properties and galaxy environments, and will use them to test star-formation and galaxy-formation models.

We would like to thank, among others, Andrew Cardwell, Ignacio Trujillo, Alister Graham, Bo Milvang-Jensen, and Bruce Elmegreen for helpful and stimulating conversations. We are also grateful to Juan Carlos Vega Beltrán for his help with the Nordic Optical Telescope observations, and to Paul Schechter for the MDM observations of NGC 4612. Gabriel Pérez helped prepare Figure 5. Finally, an anonymous referee made several helpful suggestions.

P.E. was supported by DFG Priority Program 1177. M.P. was (partly) supported by a Marie Curie Intra-European Fellowship within the 6th European Community Framework Programme. This work was also supported by grants No. AYA2004-08251-CO2-01 from the Spanish Ministry of Education and Science and P3/86 of the Instituto de Astrofísica de Canarias. P.E. and M.P. acknowledge the hospitality of the IAC, where much of the initial research was carried out.

This research is based in part on data from the ING Archive, and on observations made with both the Isaac Newton Group of Telescopes, operated on behalf of the UK Particle Physics and Astronomy Research Council (PPARC) and the Nederlandse Organisatie voor Wetenschappelijk Onderzoek (NWO) on the island of La Palma, and the Nordic Optical Telescope, operated on

the island of La Palma jointly by Denmark, Finland, Iceland, Norway, and Sweden. Both the ING and the NOT are part of the Spanish Observatorio del Roque de los Muchachos of the Instituto de Astrofísica de Canarias. We also used images from the Barred and Ringed Spirals (BARS) database, for which time was awarded by the Comité Científico Internacional of the Canary Islands Observatories.

The data from the NOT presented here have been taken using ALFOSC, which is owned by the Instituto de Astrofísica de Andalucía (IAA) and operated at the Nordic Optical Telescope under agreement between IAA and the NBIfAFG of the Astronomical Observatory of Copenhagen.

Funding for the creation and distribution of the SDSS Archive has been provided by the Alfred P. Sloan Foundation, the Participating Institutions, the National Aeronautics and Space Administration, the National Science Foundation, the U.S. Department of Energy, the Japanese Monbukagakusho, and the Max Planck Society. The SDSS Web site is <http://www.sdss.org/>.

The SDSS is managed by the Astrophysical Research Consortium (ARC) for the Participating Institutions. The Participating Institutions are The University of Chicago, Fermilab, the Institute for Advanced Study, the Japan Participation Group, The Johns Hopkins University, the Korean Scientist Group, Los Alamos National Laboratory, the Max-Planck-Institute for Astronomy (MPIA), the Max-Planck-Institute for Astrophysics (MPA), New Mexico State University, University of Pittsburgh, University of Portsmouth, Princeton University, the United States Naval Observatory, and the University of Washington.

Finally, this research has made extensive use of the Lyon-Meudon Extragalactic Database (LEDa; <http://leda.univ-lyon1.fr>) and of the NASA/IPAC Extragalactic Database (NED); the latter is operated by the Jet Propulsion Laboratory, California Institute of Technology, under contract with the National Aeronautics and Space Administration.

REFERENCES

- Adamson, A. J., Adams, D. J., & Warwick, R. S. 1987, *MNRAS*, 224, 367
- Adelman-McCarthy, J. K., et al. 2007, *ApJS*, in press (arXiv:0707.3380)
- Ajhar, E. A., Tonry, J. L., Blakeslee, J. P., Riess, A. G., & Schmidt, B. P. 2001, *ApJ*, 559, 584
- Aladro, R., Gutiérrez, L., Erwin, P., & Beckman, J. E. 2007, in *Pathways through an Eclectic Universe*, eds. J. H. Knapen, T. J. Mahoney, & A. Vazdekis (San Francisco: ASP Conference Series), in press.
- Athanassoula, E., & Misiriotis, A. 2002, *MNRAS*, 330, 35
- Barton, I. J., & Thompson, L. A. 1997, *AJ*, 114, 655
- Battaner, E., Florido, E., & Jiménez-Vicente, J. 2002, *A&A*, 388, 213
- Baggett, W. E., Baggett, S. M., & Anderson, K. S. J. 1998, *AJ*, 116, 1626
- Bland-Hawthorn, J., Vlajić, M., Freeman, K. C., & Draine, B. T. 2005, *ApJ*, 629, 239
- Buta, R. 1986, *ApJS*, 61, 609
- Buta, R. 1995, *ApJS*, 96, 39
- Buta, R., & Crocker, D. A. 1993, *AJ*, 105, 1344
- Buta, R., & Combes, F. 1996, *Fundamentals of Cosmic Physics*, 17, 95
- Byun, Y.-I., et al. 1996, *AJ*, 111, 1889
- Debattista, V. P., Mayer, L., Carollo, C. M., Moore, B., Wadsley, J., & Quinn, T. 2006, *ApJ*, 645, 209
- Eskridge, P. B., et al. 2000, *AJ*, 119, 536
- de Grijs, R., Kregel, M., & Wesson, K. H. 2001, *MNRAS*, 324, 1074
- de Jong, R. S., & van der Kruit, P. C. 1994, *A&AS*, 106, 451
- de Vaucouleurs, G. 1959, *Handbuch der Physik*, 53, 311
- de Vaucouleurs, G., & de Vaucouleurs, A. 1964, *Reference Catalogue of Bright Galaxies* (Austin: University of Texas)
- de Vaucouleurs, G., de Vaucouleurs, A., Corwin, H. G., Buta, R. J., Paturel, G., & Fouqué, P. 1991, *Third Reference Catalogue of Bright Galaxies* (New York: Springer-Verlag) (RC3)
- Elmegreen, B. G., & Hunter, D. A. 2006, *ApJ*, 636, 712
- Erwin, P. 2005, *MNRAS*, 364, 283
- Erwin, P. 2007a, in prep
- Erwin, P. 2007b, in prep
- Erwin, P., & Sparke, L. S. 1999, *ApJ*, 512, L37
- Erwin, P., & Sparke, L. S. 2003, *ApJS*, 146, 299
- Erwin, P., Vega Beltrán, J. C., Graham, A. W., & Beckman, J. E. 2003, *ApJ*, 597, 929
- Erwin, P., Beckman, J. E., & Pohlen, M. 2005, *ApJ*, 626, L81
- Erwin, P., Pohlen, M., & Beckman, J. E. 2007, in prep
- Eskridge, P. B., et al. 2002, *ApJS*, 143, 73
- Ferguson, A. M. N., & Clarke, C. J. 2001, *MNRAS*, 325, 781
- Forbes, D. A. 1996, *AJ*, 112, 1409
- Freedman, W. L., et al. 2001, *ApJ*, 553, 47
- Freeman, K. C. 1970, *ApJ*, 160, 811
- Frei, Z., Guhathakurta, P., Gunn, J. E., & Tyson, J. A. 1996, *AJ*, 111, 174

- Garrido, O., Marcelin, M., Amram, P., Balkowski, C., Gach, J. L., & Boulesix, J. 2005, *MNRAS*, 362, 127
- Gavazzi, G., Boselli, A., Donati, A., Franzetti, P., & Scodreggio, M. 2003, *A&A*, 400, 451
- Governato, F., Willman, B., Mayer, L., Brooks, A., Stinson, G., and Valenzuela, O., Wadsley, J., & Quinn, T. 2007, *MNRAS*, 374, 1479
- Gutiérrez, L., Erwin, P., Aladro, R., Beckman, J. E., & Pohlen, M. 2007, in prep
- Gunn, J. E., et al. 1998, *AJ*, 116, 3040
- Gunn, J. E., et al. 2006, *AJ*, 131, 2332
- Holtzman, J. A., Burrows, C. J., Casertano, S., Hester, J. J., Trauger, J. T., Watson, A. M., & Worthey, G. 1995, *PASP*, 107, 1065
- Hunter, D. A., & Elmegreen, B. G. 2005, *ApJS*, 162, 49
- Ibata, R., Chapman, S., Ferguson, A. M. N., Lewis, G., Irwin, M., & Tanvir, N. 2005, *ApJ*, 634, 287
- Kent, S. M., & Glauddell, G. 1989, *AJ*, 98, 1588
- Kennicutt, R. C. 1989, *ApJ*, 344, 685
- Kennicutt, R. C., & Edgar, B. K. 1986, *ApJ*, 300, 132
- Kennicutt, R. C. et al. 2003, *PASP*, 115, 928
- Koopmann, R. A., & Kenney, J. D. P. 1998, *ApJ*, 497, L75
- Kormendy, J. 1977, *ApJ*, 214, 359
- Kormendy, J. 1979, *ApJ*, 227, 714
- Kormendy, J. 1984, *ApJ*, 286, 132
- Krumm, N., & Shane, W. W. 1982, *A&A*, 116, 237
- Landolt, A. U., 1992, *AJ*, 104, 340
- Lauer, T. R., et al. 1995, *AJ*, 110, 2622
- Laurikainen, E., Salo, H., Buta, R., & Vasylyev, S. 2004, *MNRAS*, 355, 1251
- Laurikainen, E., Salo, H., & Buta, R. 2005, *MNRAS*, 362, 1319
- Lourenso, S., & Beckman, J. E. 2001, *Ap&SS*, 276, 1161
- MacArthur, L. A., Courteau, S., & Holtzman, J. A. 2003, *ApJ*, 582, 689
- Matthews, L. D., & Gallagher, J. S. 1997, *AJ*, 114, 1899
- Mei, S., Blakeslee, J. P., Côté, P., Tonry, J. L., West, M. J., Ferrarese, L., Jordán, A., Peng, E. W., Anthony, A., & Merritt, D. 2007, *ApJ*, 655, 144
- Menéndez-Delmestre, K., Sheth, K., Schinnerer, E., Jarrett, T. H., & Scoville, N. Z. 2007, *ApJ*, 657, 790
- Navarro, J. F. & White, S. D. M. 1994, *MNRAS*, 267, 401
- Nilson, P. 1973, *Uppsala General Catalog of Galaxies*, Uppsala Astron. Obs. Annals, 5, 1
- Phillips, S., Evans, R., Davies, J. I., & Disney, M. J. 1991, *MNRAS*, 253, 496
- Pohlen, M., & Trujillo, I. 2006, *A&A*, 454, 759
- Pohlen, M., Dettmar, R.-J., Lütticke, R., & Aronica, G. 2002, *A&A*, 392, 807
- Pohlen, M., Beckman, J. E., S. Hüttemeister, S., Knapen, J. H., Erwin, P., & Dettmar, R.-J. 2004, *Penetrating Bars through Masks of Cosmic Dust: The Hubble Tuning Fork Strikes a New Note*, ed. D. L. Block, I. Puerari, K. C. Freeman, R. Groess, & E. K. Block (Dordrecht: Springer), 731
- Prugniel, P., & Heraudeau, P. 1998, *A&AS*, 128, 299
- Riess, A. G., et al. 2005, *ApJ*, 627, 579
- Robertson, B., Yoshida, N., Springel, V., & Hernquist, L. 2004, *ApJ*, 606, 32
- Saha, A., et al. 2001, *ApJ*, 562, 314
- Sandage, A. 1961, *The Hubble Atlas of Galaxies* (Washington, D.C.: Carnegie Institution)
- Sandage, A., & Visvanathan, N. 1978, *ApJ*, 223, 707
- Schaye, J. 2004, *ApJ*, 609, 667
- Slyz, A. D., Devriendt, J. E. G., Silk, J., & Burkert, A. 2002, *MNRAS*, 333, 894
- Smith, J. A., et al. 2002, *AJ*, 123, 2121
- Stetson, P. B., & Gibson, B. K. 2001, *MNRAS*, 328, L1
- Tonry, J. L., Dressler, A., Blakeslee, J. P., Ajhar, E. A., Fletcher, A. B., Luppino, G. A., Metzger, M. R., & Moore, C. B. 2001, *ApJ*, 546, 681
- Valenzuela, O., & Klypin, A. 2003, *MNRAS*, 345, 406
- van den Bergh, S. 1976, *ApJ*, 206, 883
- van der Kruit, P. C., 1979, *A&AS*, 38, 15
- van der Kruit, P. C., 1987, *A&A*, 173, 59
- van der Kruit, P. C., & Searle, L., 1981a, *A&A*, 95, 105
- van der Kruit, P. C., & Searle, L., 1981b, *A&A*, 95, 116
- van Driel, W., & Buta, R. J. 1991, *A&A*, 245, 7
- Weiner, B. J., Williams, T. B., van Gorkom, J. H., & Sellwood, J. A. 2001, *ApJ*, 546, 916
- Wozniak, H., & Pierce, M. J. 1991, *A&AS*, 88, 325
- Younger, J. D., Cox, T. J., Seth, A. C., & Hernquist, L. 2007, *ApJ*, in press (arXiv:0707.4481)
- Yoshii, Y., & Sommer-Larsen, J. 1989, *MNRAS*, 236, 779
- York, D. G., et al. 2000, *AJ*, 120, 1579
- Zhang, B., & Wyse, R. F. G. 2000, *MNRAS*, 313, 310

TABLE 1
BASIC GALAXY DATA

Name	Type (RC3)	Distance	Source	M_B	R_{25}	Outer Disk PA	Disk i	Bar Size a_ϵ	L_{bar}	R_{OR}	Source
(1)	(2)	(Mpc) (3)	(4)	(5)	($''$) (6)	($^\circ$) (7)	($^\circ$) (8)	($''$) (9)	($''$) (10)	($''$) (11)	(12)
NGC 718	SAB(s)a	22.6		-19.43	71	5	30	21	31	42	1
NGC 936	SB(rs)0 ⁺	23.0		-20.86	140	130	41	49	61		
NGC 1022	(R')SB(s)a	18.1		-19.46	72	174	24	20	24	56	1
NGC 2273	SB(r)a:	27.3		-20.11	97	50	50	21	25	66	1
NGC 2681	(R')SAB(rs)0/a	17.2		-20.20	109	140	18	52	63	68	2
NGC 2712	SB(r)b:	26.5		-19.88	87	10	59	26	28	85	3
NGC 2787	SB(r)0 ⁺	7.5		-18.20	95	109	55	43	54		
NGC 2859	(R)SB(r)0 ⁺	24.2		-20.21	128	85	32	40	50	102	1
NGC 2880	SB0 ⁻	21.9		-19.38	62	144	52	12	14		
NGC 2950	(R)SB(r)0 ⁰	14.9		-19.14	80	125	48	29	37	61	1
NGC 2962	(R)SAB(rs)0 ⁺	30.0	1	-19.71	79	7	53	32	47	66	1
NGC 3049	SB(rs)ab	20.2		-18.65	66	26	51	35	38		
NGC 3185	(R)SB(r)a	17.5		-18.61	71	140	49	35	36	75	1
NGC 3351	SB(r)b	10.0	2	-19.94	222	10	46	74	83	165	2
NGC 3368	SAB(rs)ab	10.5	2	-20.37	228	172	50	86	106	185	1
NGC 3412	SB(s)0 ⁰	11.3		-18.98	109	152	58	24	34		
NGC 3485	SB(r)b:	20.0		-19.03	69	5	26	21	25		
NGC 3489	SAB(rs)0 ⁺	12.1		-19.45	106	71	58	22	29	51	4
NGC 3504	(R)SAB(s)ab	22.3		-20.29	81	149	22	29	34	63	2
NGC 3507	SB(s)b	14.2		-19.21	102	90	27	26	30		
NGC 3729	SB(r)a	16.8		-19.35	85	174	53	28	32		
NGC 3941	SB(s)0 ⁰	12.2	3	-19.31	104	8	52	23	35		
NGC 3945	(R)SB(rs)0 ⁺	19.8		-19.94	158	158	55	56	68	135	1
NGC 3982	SAB(r)b:	20.9	4	-19.95	70	17	29	4	5	10	1
NGC 4037	SB(rs)b:	13.5		-17.79	75	150	32	29	36		
NGC 4045	SAB(r)a	26.8		-19.70	81	90	48	26	29	66	4
NGC 4102	SAB(s)b?	14.4		-19.22	91	38	55	12	18	36	1
NGC 4143	SAB(s)0 ⁰	15.9		-19.40	68	144	59	19	32		
NGC 4151	(R')SAB(rs)ab:	15.9		-20.70	189	22	20	69	95	230	3
NGC 4203	SAB0 ⁻	15.1		-19.21	102	11	28	13	46		
NGC 4245	SB(r)0/a	12.0	5	-18.28	87	173	38	41	46		
NGC 4267	SB(s)0 ⁻ ?	15.8	6	-19.32	97	127	25	20	29		
NGC 4314	SB(rs)a	12.0	5	-19.12	125	65	25	74	88	109	2
NGC 4319	SB(r)ab	23.5		-19.26	89	135	42	16	18	38	1
NGC 4340	SB(r)0 ⁺	16.5	7	-19.07	105	101	56	67	82		
NGC 4371	SB(r)0 ⁺	17.0	6	-19.55	119	86	58	64	75		
NGC 4386	SAB0 ⁰ :	27.0		-19.68	74	140	48	25	36		
NGC 4477	SB(s)0 ⁰ ?	16.5	7	-19.86	114	80	33	29	43		
NGC 4531	SB0 ⁺ :	15.2	3	-18.67	93	154	49	10	16		
NGC 4596	SB(r)0 ⁺	16.5	7	-19.80	119	120	42	62	68		
NGC 4608	SB(r)0 ⁰	16.5	7	-19.19	97	100	36	54	60		
NGC 4612	(R)SAB0 ⁰	16.6	6	-19.19	74	143	44	22	26	67	1
NGC 4643	SB(rs)0/a	18.3		-19.85	93	53	38	63	78		
NGC 4665	SB(s)0/a	10.9		-18.87	114	120	26	49	71	72	1
NGC 4691	(R)SB(s)0/a	15.1		-19.43	85	30	38	35	53	81	1
NGC 4699	SAB(rs)b	18.9		-21.37	114	37	42	13	16	81	1
NGC 4725	SAB(r)ab	12.4	2	-20.69	321	40	42	119	127	300	1
NGC 4754	SB(r)0 ⁻ :	16.8	3	-19.78	137	22	62	44	52		
NGC 4995	SAB(r)b	23.6		-20.41	74	93	47	22	27		
NGC 5338	SB0 ⁰ :	12.8		-16.70	76	95	66	17	23		
NGC 5377	(R)SB(s)a	27.1		-20.29	111	25	59	67	77	110	1
NGC 5701	(R)SB(rs)0/a	21.3		-19.97	128	45	20	41	60	102	1
NGC 5740	SAB(rs)b	22.0		-19.67	89	161	60	18	20		
NGC 5750	SB(r)0/a	26.6		-19.94	91	65	62	37	41		
NGC 5806	SAB(s)b	19.2		-19.67	93	166	58	38	39		
NGC 5832	SB(rs)b?	9.9		-17.15	111	45	55	43	49		
NGC 5957	(R')SAB(r)b	26.2		-19.36	85	100	15	24	27		
NGC 6012	(R)SB(r)ab:	26.7		-19.78	63	45	33	34	41		
NGC 6654	(R')SB(s)0/a	28.3		-19.65	79	0	44	27	39	56	1
NGC 7177	SAB(r)b	16.8		-19.79	93	83	48	14	16		
NGC 7280	SAB(r)0 ⁺	24.3		-19.16	66	74	50	10	23		
NGC 7743	(R)SB(s)0 ⁺	20.7		-19.49	91	105	28	31	37	117	1
IC 676	(R)SB(r)0 ⁺	19.4		-18.42	74	15	47	15	21	55	4
IC 1067	SB(s)b	22.2		-18.82	64	120	44	21	21		
UGC 3685	SB(rs)b	26.8		-19.51	99	119	31	25	27		
UGC 11920	SB0/a	18.0		-19.71	72	50	52	26	39		

NOTE. — Col. (1) Galaxy name; (2) Hubble type from RC3; (3) distance in Mpc, from LEDA unless otherwise specified; (4) source for distance if not from LEDA: 1 = Ajhar et al. (2001), 2 = Freedman (2001), 3 = Tonry et al. (2001), 4 = Riess et al. (2005), 5 = Forbes (1996), 6 = Mei et al. (2007), 7 = mean Virgo Cluster distance from Mei et al.; (5) absolute blue magnitude, based on B_{tc} in LEDA; (6) one-half of the corrected $\mu_B = 25$ magnitude diameter D_0 from RC3; (7) and (8) position angle and inclination of the outer disk, from Erwin (2005); (9) and (10) lower and upper limits on the bar length, from Erwin (2005), deprojected; (11) semi-major axis of the outer ring, if any; (12) source for outer-ring measurement: 1 = de Vaucouleurs & de Vaucouleurs (1964), 2 = Buta &

TABLE 2
INT-WFC PHOTOMETRIC CALIBRATIONS

Date	Filter	Z	k_1	k_2
2003 Sept. 19	B	24.683	-0.165	0.033
2003 Sept. 19	R	24.760	-0.090	-0.110
2004 March 14	B
2004 March 14	R	24.682	-0.116	0.006
2004 March 15	B	24.469	-0.085	0.132
2004 March 15	R	24.614	-0.122	0.071
2004 March 16	B	24.833	-0.263	0.059
2004 March 16	R	24.776	-0.115	-0.057
2004 March 17	B	24.767	-0.255	0.074
2004 March 17	R	26.649	-0.117	0.027

NOTE. — Photometric parameters for our INT-WFC observations; the zero point for a given night is $Z + k_1X + k_2(B - R)$, where X is the airmass and $B - R$ is the color of the object. See Section 2.4 for more details.

TABLE 3
OBSERVATIONS AND CALIBRATIONS

Galaxy	Telescope/Instrument	Date	t_{exp} (s)	Filter	Calibration	Notes
NGC 718	INT-WFC	2003 Sep 19	10200	r	standards	
NGC 936	INT-WFC	2003 Sep 21	600	r	PH98	
	SDSS	...	54	r	SDSS	
NGC 1022	WIYN	1997 Mar 2	300	R	...	1
NGC 2273	WIYN	1995 Dec 27	300	R	INT-WFC	
	INT-WFC	2004 Mar 15	120	r	standards	
NGC 2681	WIYN	1997 Mar 2	300	R	SDSS	
	SDSS	...	54	r	SDSS	
NGC 2712	INT-WFC	2000 Mar 29	150	R	SDSS	2
	SDSS	...	54	r	SDSS	
NGC 2787	WIYN	1995 Dec 26	240	R	JKT	
	JKT	2001 Jan 29	2000	R	standards	2
NGC 2859	SDSS	...	54	r	SDSS	
	WIYN	1995 Dec 26	180	R	...	
NGC 2880	WIYN	1997 Mar 2	300	R	INT-WFC	
	INT-WFC	2004 Mar 16	1200	r	standards	
NGC 2950	SDSS	...	54	r	SDSS	
NGC 2962	WIYN	1997 Mar 2	300	R	PH98	
	SDSS	...	54	r	SDSS	
NGC 3049	SDSS	...	54	r	SDSS	
	NOT	2002 Apr 18	600	R	...	
NGC 3185	SDSS	...	54	r	SDSS	
NGC 3351	SDSS	...	54	r	SDSS	
NGC 3368	SDSS	...	54	r	SDSS	
NGC 3412	INT-WFC	2004 Mar 15	2400	r	standards	
	SDSS	...	54	r	SDSS	
NGC 3485	NOT	2002 Apr 18	600	R	PH98	
NGC 3489	INT-WFC	2004 Mar 14	1200	r	standards	
	SDSS	...	54	r	SDSS	
NGC 3504	JKT	1998 Mar 2	600	R	PH98	2
NGC 3507	SDSS	...	54	r	SDSS	
	NOT	2002 Apr 18	600	R	...	
NGC 3729	INT-WFC	2004 Mar 16	120	r	standards	
	SDSS	...	54	r	SDSS	
NGC 3941	INT-WFC	2004 Mar 15	120	r	standards	
	SDSS	...	54	r	SDSS	
NGC 3945	INT-WFC	2004 Mar 15	120	r	standards	
	SDSS	...	54	r	SDSS	
NGC 3982	SDSS	...	54	r	SDSS	
NGC 4037	INT-WFC	2004 Mar 16	120	r	standards	
	SDSS	...	54	r	SDSS	
NGC 4045	SDSS	...	54	r	SDSS	
	INT-WFC	2004 Mar 16	120	r	standards	
	WIYN	1998 Mar 21	300	R	...	
NGC 4102	INT-WFC	2004 Mar 17	1200	r	standards	
	SDSS	...	54	r	SDSS	
NGC 4143	INT-WFC	2004 Mar 16	120	r	standards	
	SDSS	...	54	r	SDSS	
NGC 4151	INT-PFCU	1996 Feb 11	600	R	SDSS	3
	SDSS	...	54	r	SDSS	
NGC 4203	SDSS	...	54	r	SDSS	
	INT-WFC	2004 Mar 16	30	r	standards	
NGC 4245	INT-WFC	2004 Mar 14	1200	r	standards	
	SDSS	...	54	r	SDSS	
NGC 4267	SDSS	...	54	r	SDSS	
NGC 4314	INT-WFC	2004 Mar 17	60	r	standards	
NGC 4319	JKT	1998 Dec 24	3000	R	...	1,2
NGC 4340	SDSS	...	54	r	SDSS	
NGC 4371	INT-WFC	2004 Mar 16	1200	r	standards	
	SDSS	...	54	r	SDSS	
NGC 4386	INT-WFC	2004 Mar 17	60	r	standards	
NGC 4477	SDSS	...	54	r	SDSS	
NGC 4531	SDSS	...	54	r	SDSS	
NGC 4596	INT-PFCU	1996 Feb 11	600	R	SDSS	3
	SDSS	...	54	r	SDSS	
NGC 4608	SDSS	...	54	r	SDSS	
NGC 4612	MDM	1996 Mar 13	300	R	SDSS	
	SDSS	...	54	r	SDSS	
NGC 4643	INT-WFC	2004 Mar 17	60	r	standards	
NGC 4665	SDSS	...	54	r	SDSS	
NGC 4691	INT-WFC	2004 Mar 17	60	r	standards	
NGC 4699	NOT	2001 Apr 10	600	R	PH98	4

TABLE 3
CONTINUED

Galaxy	Telescope/Instrument	Date	t_{exp} (s)	Filter	Calibration	Notes
NGC 4725	SDSS	...	54	r	SDSS	
NGC 4754	SDSS	...	54	r	SDSS	
NGC 4995	INT-WFC	2004 Mar 17	600	r	standards	5
	NOT	2001 Apr 10	600	R	...	
NGC 5338	INT-WFC	2004 Mar 15	600	r	standards	
	SDSS	...	54	r	SDSS	
NGC 5377	SDSS	...	54	r	SDSS	
NGC 5701	Lowell	1989 Apr 1	600	R	PH98	6
NGC 5740	INT-WFC	2004 Mar 16	600	r	standards	
	SDSS	...	54	r	SDSS	
NGC 5750	INT-WFC	2004 Mar 16	120	r	standards	
NGC 5806	SDSS	...	54	r	SDSS	
	INT-WFC	2004 Mar 17	600	r	standards	
NGC 5832	INT-WFC	2004 Mar 16	600	r	standards	
NGC 5957	SDSS	...	54	r	SDSS	
	NOT	2002 Apr 18	600	R	...	
NGC 6012	INT-WFC	2004 Mar 15	600	r	standards	
NGC 6654	INT-WFC	2003 Sep 21	1200	r	INT-WFC	7
	INT-WFC	2004 Mar 16	600	r	standards	
NGC 7177	INT-WFC	2000 Jul 31	1200	R	PH98	2
NGC 7280	WIYN	1996 Oct 10	300	R	PH98	
	INT-WFC	2003 Sep 20	10200	r	PH98	
NGC 7743	WIYN	1996 Oct 9	300	R	PH98	4
IC 676	WIYN	1997 Mar 2	300	R	INT-WFC	
	INT-WFC	2004 Mar 15	120	r	standards	
IC 1067	SDSS	...	54	r	SDSS	
UGC 3685	INT-WFC	2004 Mar 15	600	r	standards	
UGC 11920	WIYN	1996 Jun 16	300	R	...	1

NOTE. — For each galaxy, the *first* line lists the main data source, used for generating the surface-brightness profile; subsequent lines list any additional observations/sources used for comparison, calibration, etc. We do not list the observation date for SDSS images. t_{exp} = cumulative exposure time in seconds. Filter = filter used for observations (note that all calibrations are in Cousins R). Calibration sources: PH98 = aperture photometry from the compilation of Prugniel & Heraudeau (1998); SDSS = standard SDSS photometric calibration, converted to Cousins R as described in the text. Notes: 1. No photometric calibration possible. 2. Archival data. 3. Data from BARS Project; profile combines 20s and 600s exposures. 4. Uncertain calibration. 5. Profile at $r < 14''$ is from higher-resolution, unsaturated NOT image, scaled to match INT-WFC image. 6. Image from Frei et al. (1996). 7. Profile from 2003 observations is better quality; calibrated using 2004 observation.

TABLE 4
OUTER DISK CLASSIFICATIONS AND MEASUREMENTS

Galaxy	Profile Type	h_i ($''$)	h_o ($''$)	R_{brk} ($''$)	$\mu_{0,i}$	$\mu_{0,o}$	μ_{brk}	Notes
NGC 718	II.o-OLR	39.9	17.1	40.5	20.88	19.34	22.0	
NGC 936	II.o-OLR(?)	51.5	27.4	95.0	20.04	18.29	22.1	
NGC 1022	I	23.8	...	>150	1
NGC 2273	II.o-CT	30.0	14.0	98.4	20.58	16.50	24.2	
NGC 2681	I	27.5	...	>180	19.70	...	> 26.6	
NGC 2712	I	19.7	...	>120	19.95	...	> 27.1	
NGC 2787	I	26.7	...	>170	19.05	...	> 24.1	
NGC 2859	II.o-OLR	...	31.9	~105	...	19.08	23.1	2,3
NGC 2880	III-s	20.0	...	~67	19.77	
NGC 2950	II.o-CT	31.8	21.7	92.1	20.41	19.00	23.7	
NGC 2962	II.o-OLR	135.8	20.9	68.4	22.33	19.32	22.9	
NGC 3049	II.o-OLR(?)	29.5	12.7	53.7	21.04	18.42	23.0	4
NGC 3185	II.o-OLR	46.3	12.5	80.9	22.39	17.37	24.4	
NGC 3351	II.o-OLR	96.5	46.6	141.1	20.69	18.94	22.3	
NGC 3368	II.o-OLR	146.8	60.6	172.3	21.14	19.28	22.4	
NGC 3412	II.o-OLR(?) + III-s	31.5	20.7	56.4	18.25	19.27	21.3	5,6
NGC 3485	I	21.9	...	>135	20.67	...	> 27.2	
NGC 3489	III-d	17.2	58.4	85.0	17.95	22.03	23.3	
NGC 3504	II.o-OLR	52.3	19.4	60.9	21.33	19.19	22.6	
NGC 3507	II.o-OLR(?)	36.7	18.9	75.1	20.31	18.22	22.6	4
NGC 3729	II.o-OLR(?)	24.3	17.2	78.5	19.52	18.02	23.0	
NGC 3941	III-s	24.2	71.9	~115	19.12	
NGC 3945	II.o-OLR	145.0	35.9	119.9	22.19	19.42	23.2	
NGC 3982	II.o-OLR + III-d	...	10.3	12.2	...	18.05	19.3	2,5
		10.3	15.3	52.9	18.06	19.83	23.6	
NGC 4037	II.o	34.2	22.2	84.7	21.24	19.85	24.0	
NGC 4045	III-d	21.9	34.2	70.0	19.82	21.35	23.5	
NGC 4102	II.o-OLR + III-s(?)	344.1	15.4	42.9	20.58	17.59	20.9	5,7
NGC 4143	III-s	14.3	...	~70	18.06	
NGC 4151	I	78.6	...	>310	22.12	...	> 26.5	
NGC 4203	II.o-OLR(?) + III-s(?)	38.0	24.4	58.1	19.96	18.95	21.7	5,8
NGC 4245	I	29.9	...	>220	20.49	...	> 27.8	
NGC 4267	I	26.1	...	>180	19.68	...	> 26.7	
NGC 4314	II.i	27.7	...	>210	19.50	...	28.9	
NGC 4319	III-d	12.0	55.8	55.0	1
NGC 4340	I	48.4	...	>220	21.47	...	> 26.5	
NGC 4371	III-d	37.1	55.4	190.0	19.96	21.81	25.6	
NGC 4386	III-s	20.5	43.0	~75	19.88	
NGC 4477	I	35.7	...	>200	19.87	...	> 26.0	4
NGC 4531	III-s	26.6	...	~125	19.81	
NGC 4596	I	39.5	...	>250	19.85	...	> 26.6	
NGC 4608	II.i	29.0	...	>175	19.85	...	> 26.6	
NGC 4612	III-d	14.2	39.3	50.0	18.67	21.26	22.7	
NGC 4643	I	53.8	...	>285	21.42	...	> 26.2	
NGC 4665	I	36.2	...	>200	19.86	...	> 25.4	
NGC 4691	III-d	29.5	47.8	125.0	19.96	21.71	24.5	
NGC 4699	III-d	12.8	35.3	41.6	16.57	18.86	20.0	
NGC 4725	II.o-OLR	184.1	55.2	268.4	22.14	18.46	24.2	
NGC 4754	I	37.6	...	>260	19.59	...	> 26.5	
NGC 4995	II.i	17.4	...	>90	18.55	...	> 24.5	
NGC 5338	II.o-CT(?)	25.2	17.1	67.3	21.03	19.65	23.9	
NGC 5377	II.o-OLR	153.6	29.8	115.7	22.70	19.01	23.5	
NGC 5701	II.o-OLR	110.0	18.3	120.0	21.74	15.70	23.1	3
NGC 5740	III-d	17.4	27.7	104.0	19.04	21.34	25.5	
NGC 5750	I	21.5	...	>160	19.26	...	> 26.8	
NGC 5806	III-d	29.6	50.6	114.0	20.05	21.76	24.2	
NGC 5832	II.i	20.9	...	>165	19.56	...	> 28.2	
NGC 5957	II.o	33.3	17.9	81.8	21.69	19.53	24.5	
NGC 6012	III-d	23.4	58.7	118.0	20.62	23.76	25.9	
NGC 6654	II.o-OLR	58.4	13.0	62.7	21.05	16.97	22.3	
NGC 7177	III-d	16.7	83.8	89.0	18.81	23.47	24.1	
NGC 7280	II.o-OLR(?)	25.4	11.2	42.5	20.20	17.90	22.1	4
NGC 7743	I	39.9	...	>145	21.08	...	> 25.1	
IC 676	I	15.6	...	>105	20.25	...	> 27.5	
IC 1067	II.o-OLR(?)	32.6	13.7	39.9	21.34	19.27	22.7	
UGC 3685	I	44.4	...	>195	22.34	...	> 27.1	
UGC 11920	II.o-OLR(?)	87.6	24.5	60.0	1

NOTE. — Classifications and measurements of surface brightness profiles. For each galaxy, we list the profile type (Section 4), the exponential scale lengths of the inner and outer parts of the profile, the break radius of Type II and III profiles, the central surface brightnesses of the fitted exponentials, and the surface brightness at the break radius. Surface brightnesses are observed values, and have not been corrected for Galactic extinction, inclination, or redshift. Note that Type I profiles by definition have no “outer” part and have only an upper limit for the break radius; some Type II profiles have non-exponential inner parts. For NGC 3982, we list values for both the inner zone (Type II.o-OLR) and the outer zone (Type III-d). Notes: 1 = no photometric calibration; 2 = non-exponential inner profile; 3 = very gradual, smooth break; 4 = tentative evidence for Type III profile at large radii; 5 = profile has multiple breaks or

TABLE 5
INNER BREAK RADII FOR TYPE II.i
PROFILES

Galaxy	R_{brk} ($''$)	Bar a_e ($''$)	Bar L_{bar} ($''$)
NGC 4314	73.5	73.8	88.0
NGC 4608	~ 47	53.8	59.9
NGC 4995	24.5	22.5	26.7
NGC 5832	~ 45	42.7	49.3

NOTE. — Break radius measurements for Type II.i profiles. These are the inner breaks, located near the end of the bar; also listed are the (deprojected) bar-radius measurements a_e and L_{bar} from Table 1. Lower limits on possible breaks at larger radii (e.g., disk truncations) are given in Table 4.

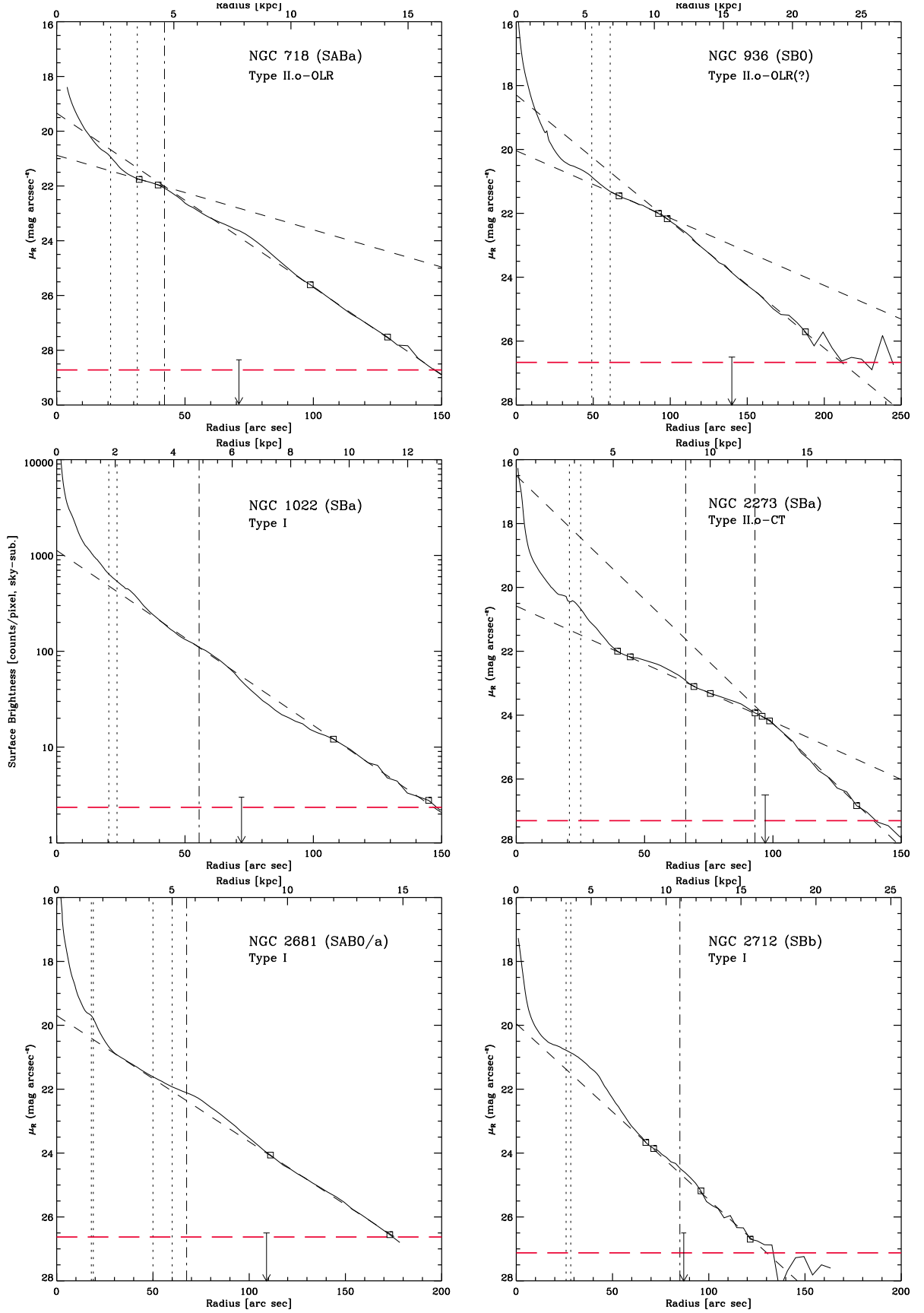


FIG. 14.— Azimuthally averaged surface brightness profiles for all the galaxies in our sample. For each galaxy, we also show lower and upper limits to the bar size (vertical dotted lines), the radius of any outer rings (vertical dot-dashed lines), and exponential fits to different parts of the profile (diagonal dashed lines; small boxes mark regions used for fits). Horizontal dashed red lines mark the sky-uncertainty limit μ_{crit} ; small arrows indicate R_{25} .

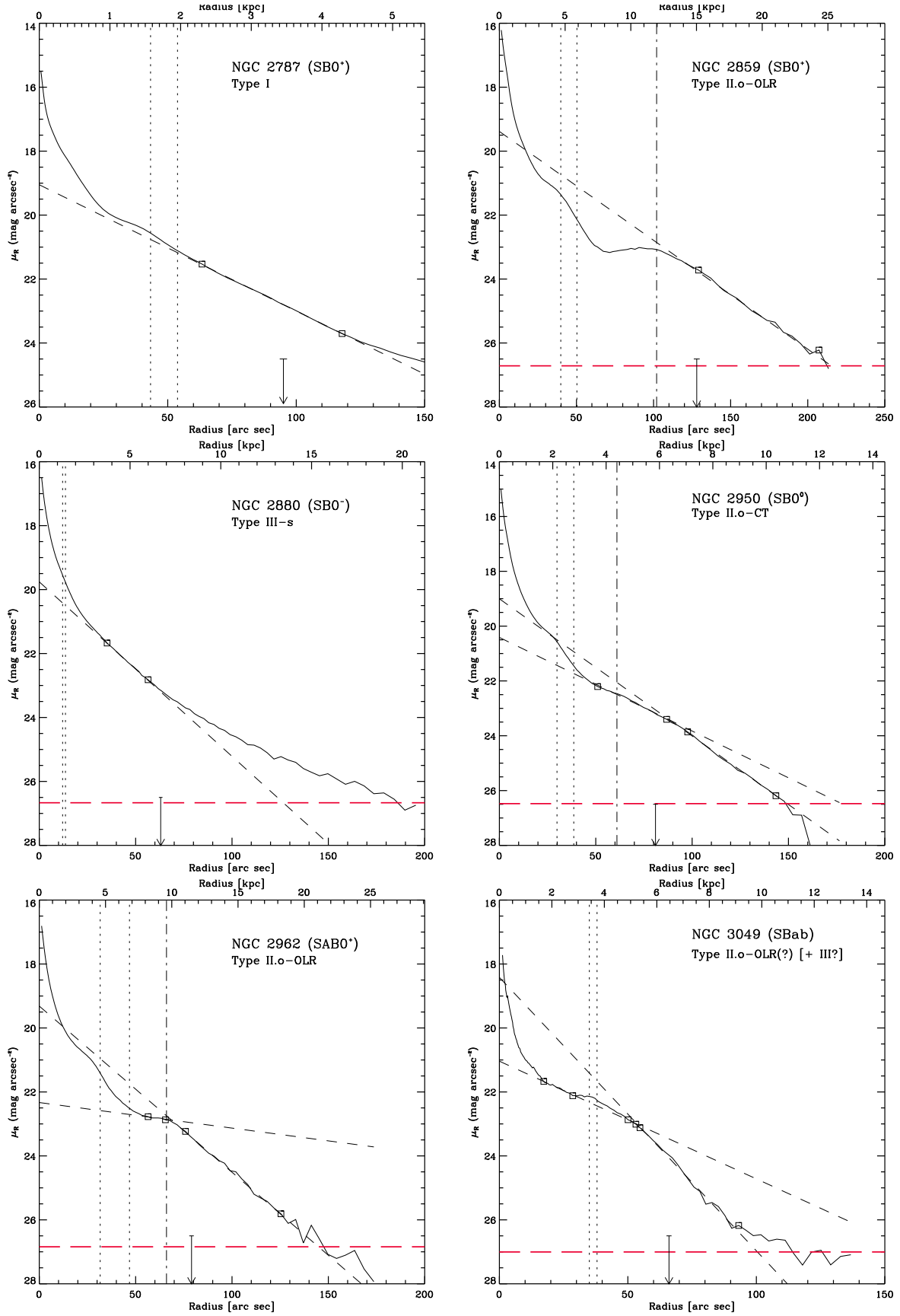


FIG. 14.— continued.

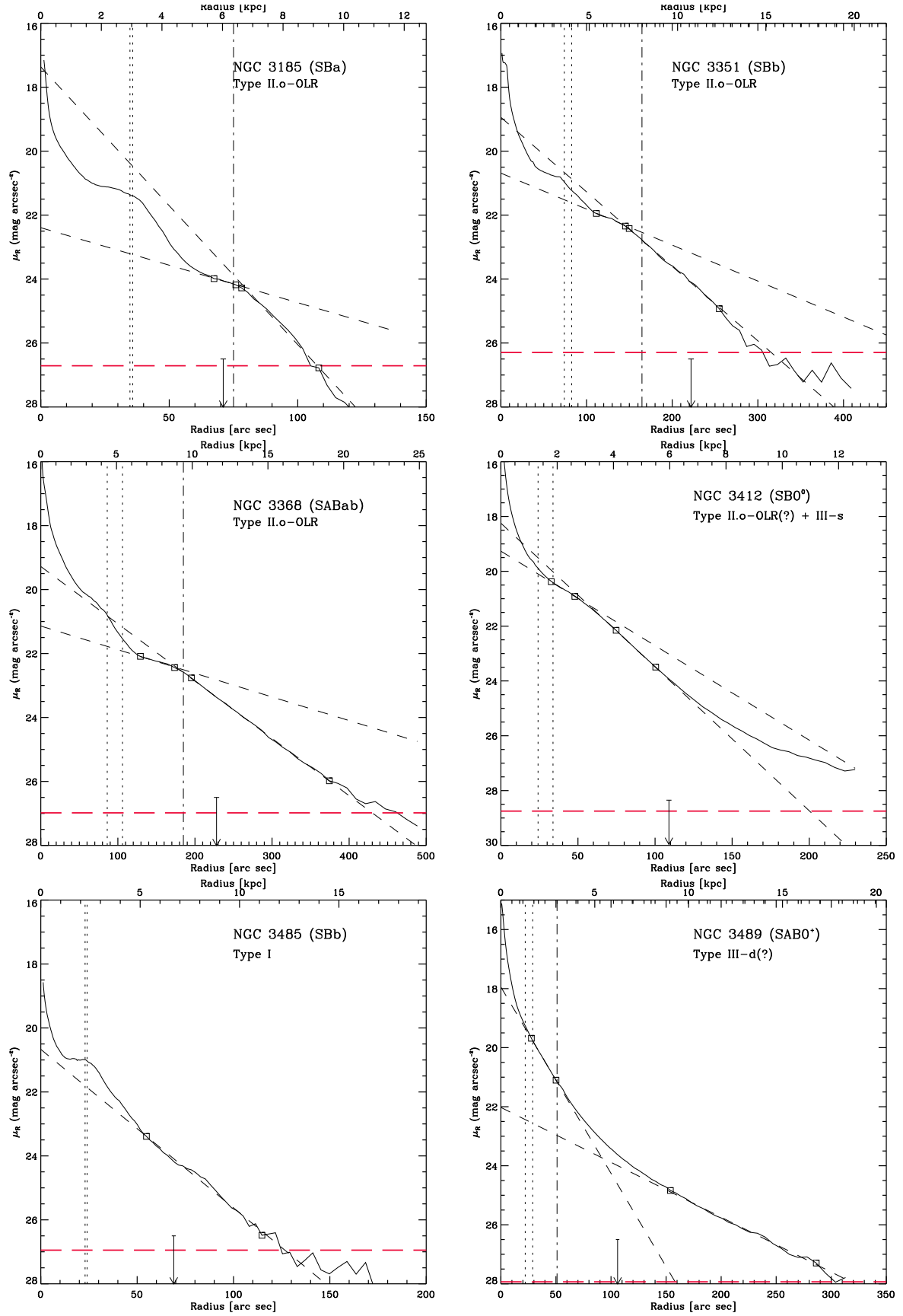


FIG. 14.— continued.

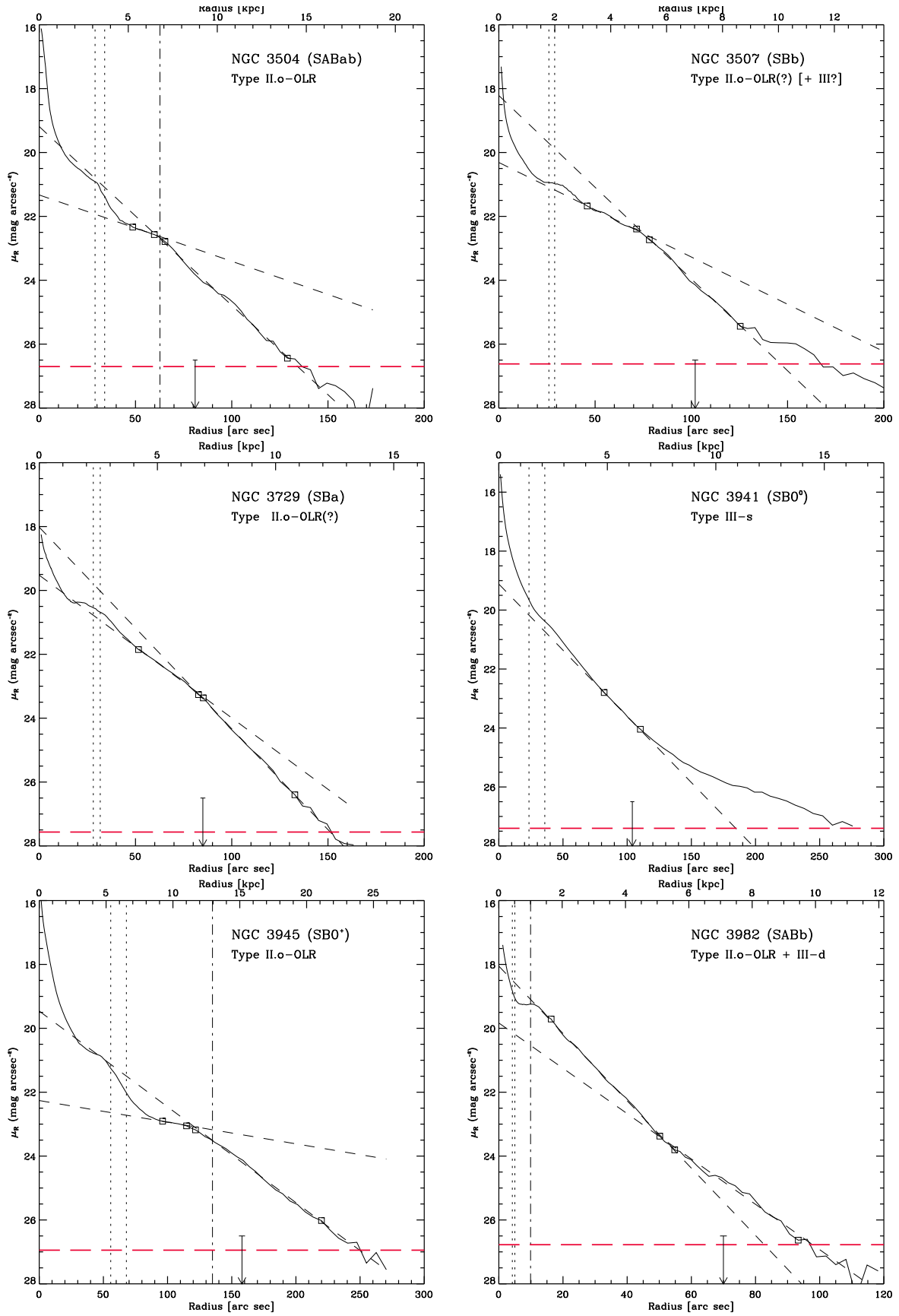


FIG. 14.— continued.

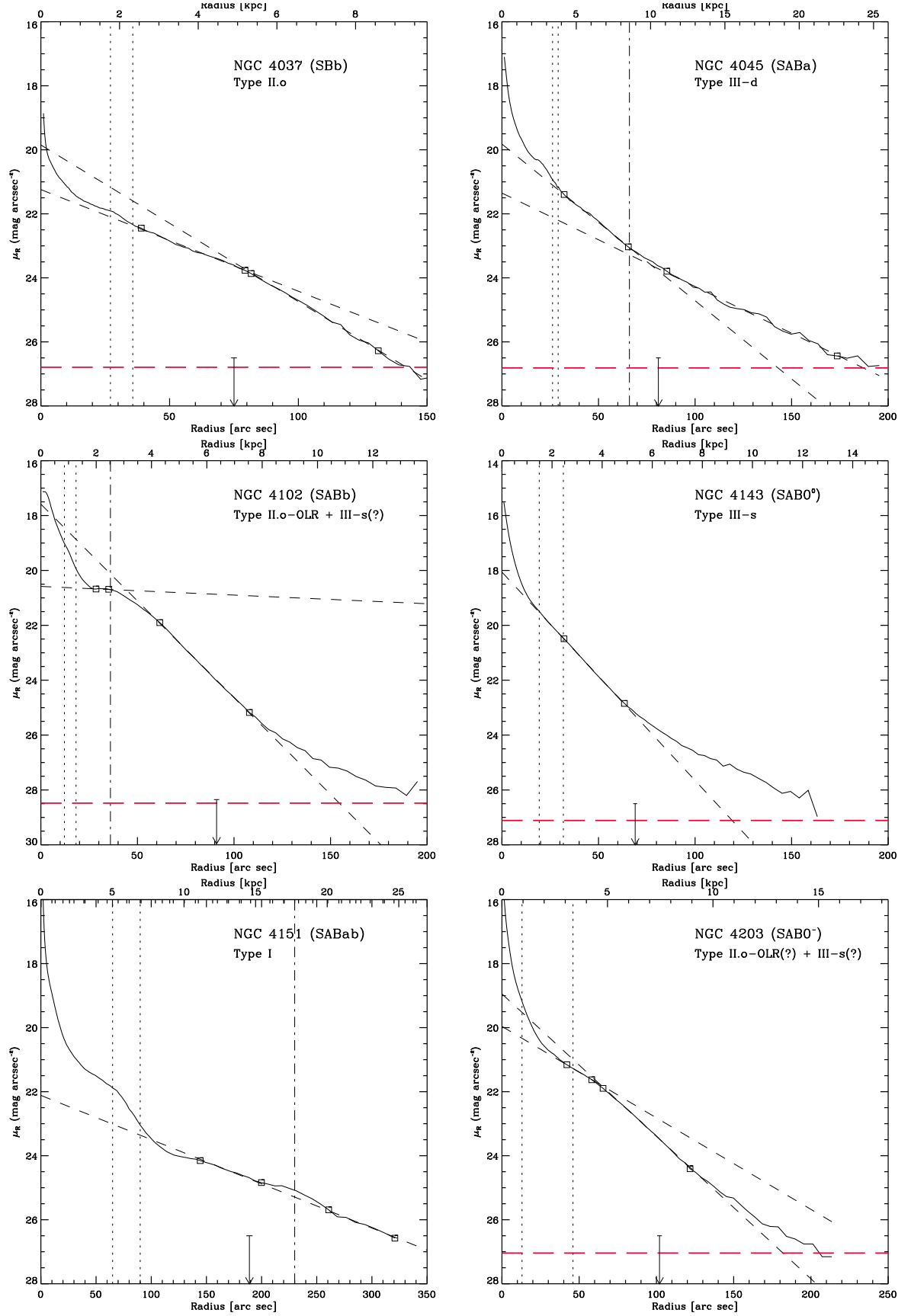


FIG. 14.— continued.

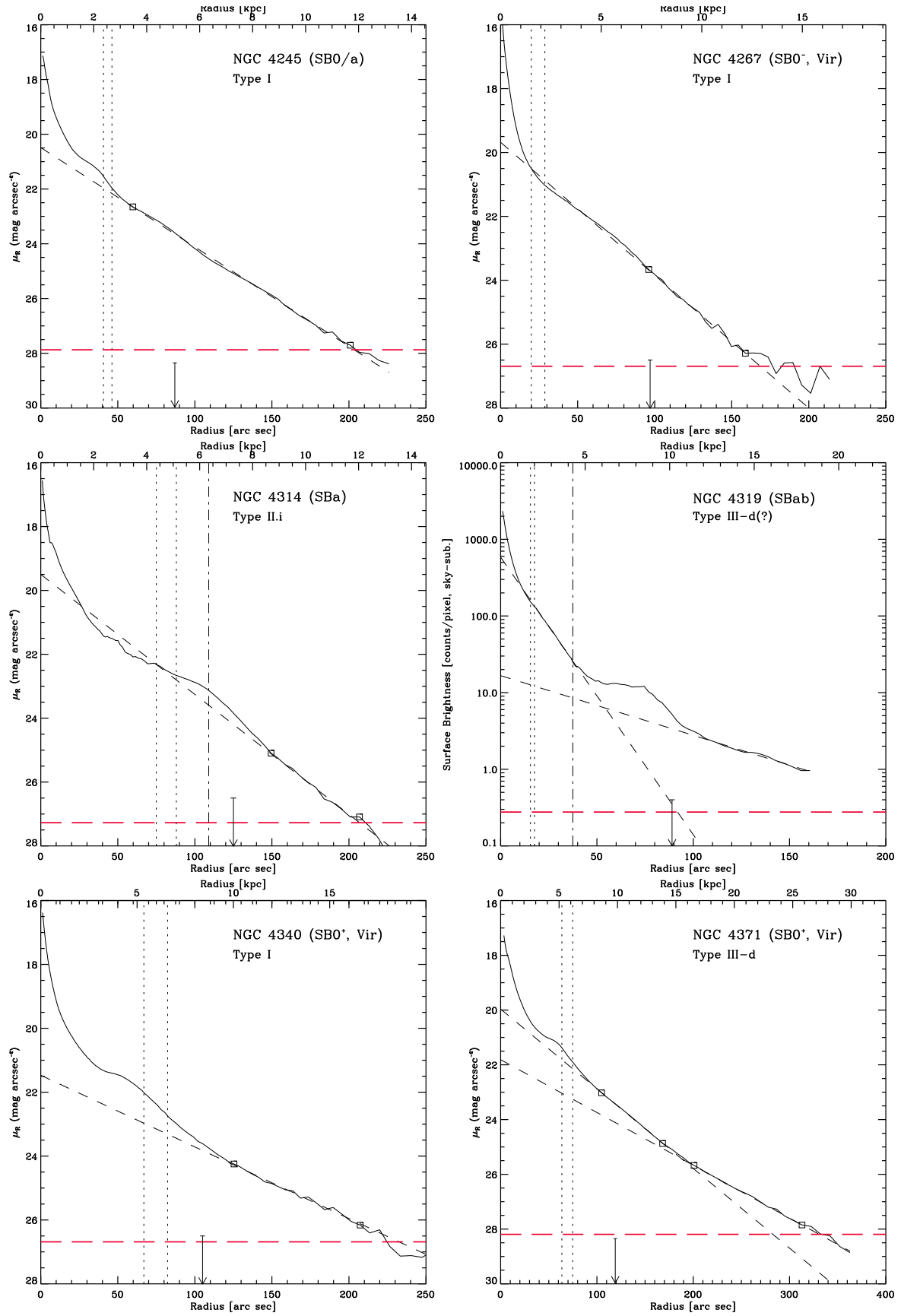


FIG. 14.— continued.

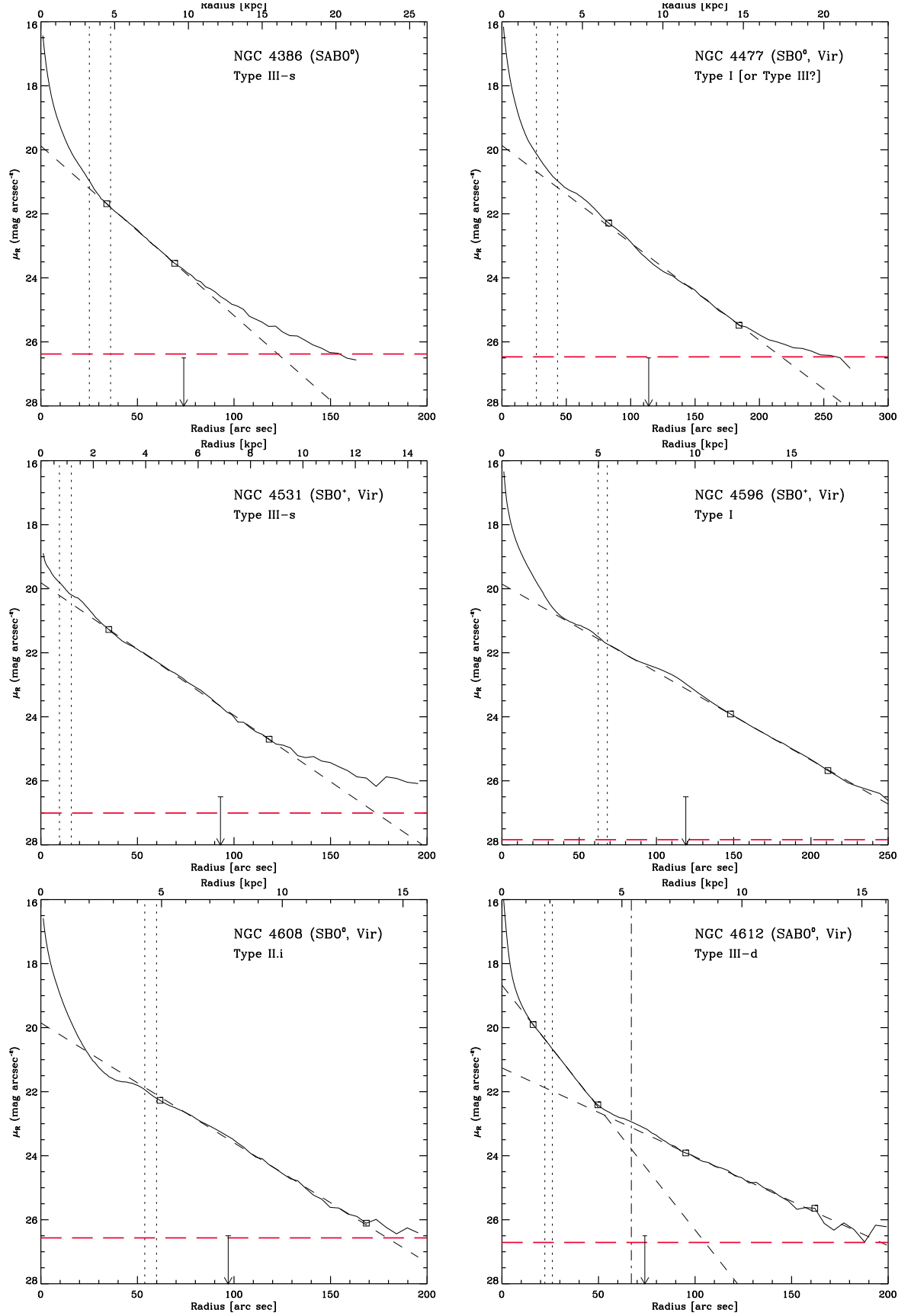


FIG. 14.— continued.

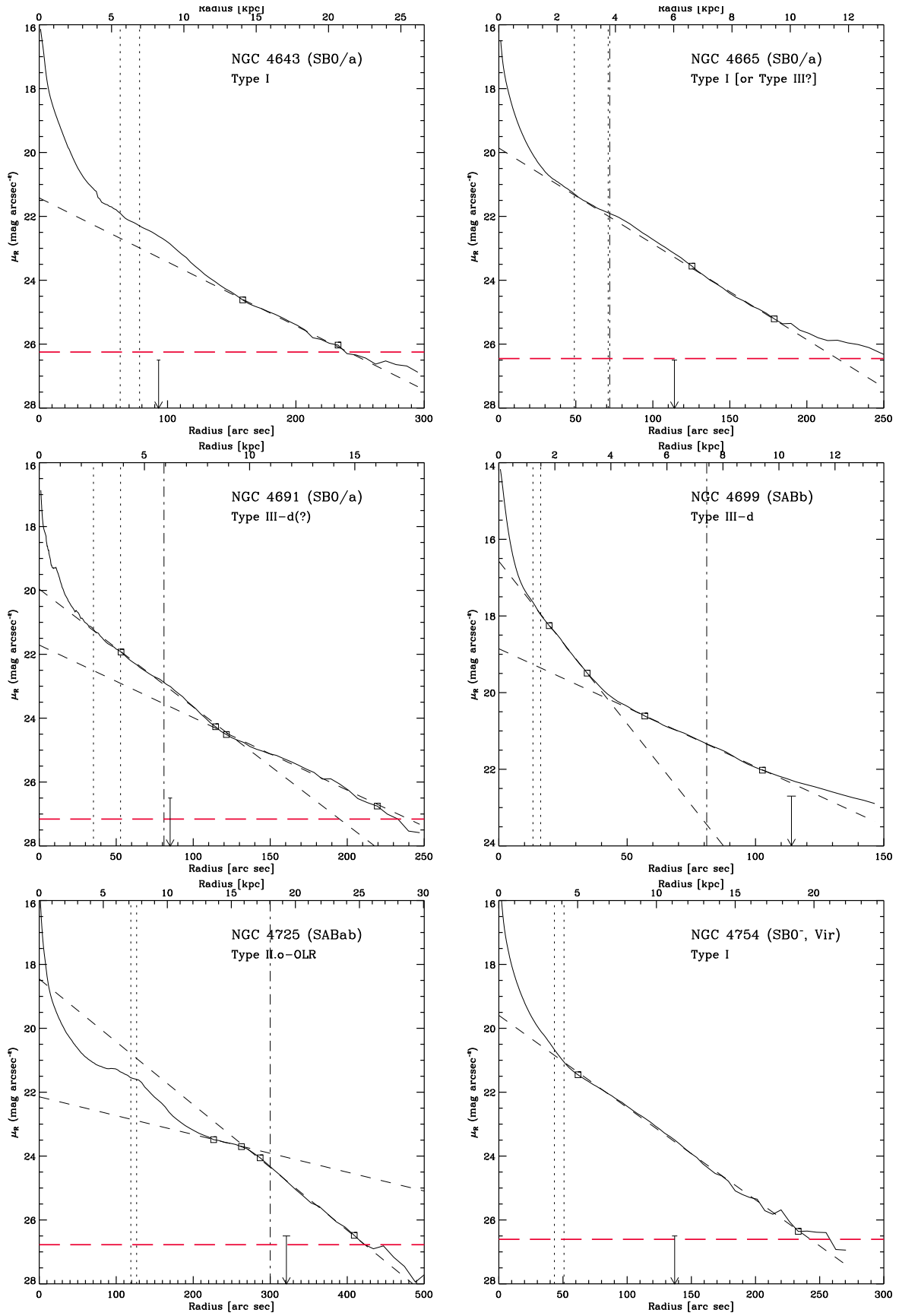


FIG. 14.— continued.

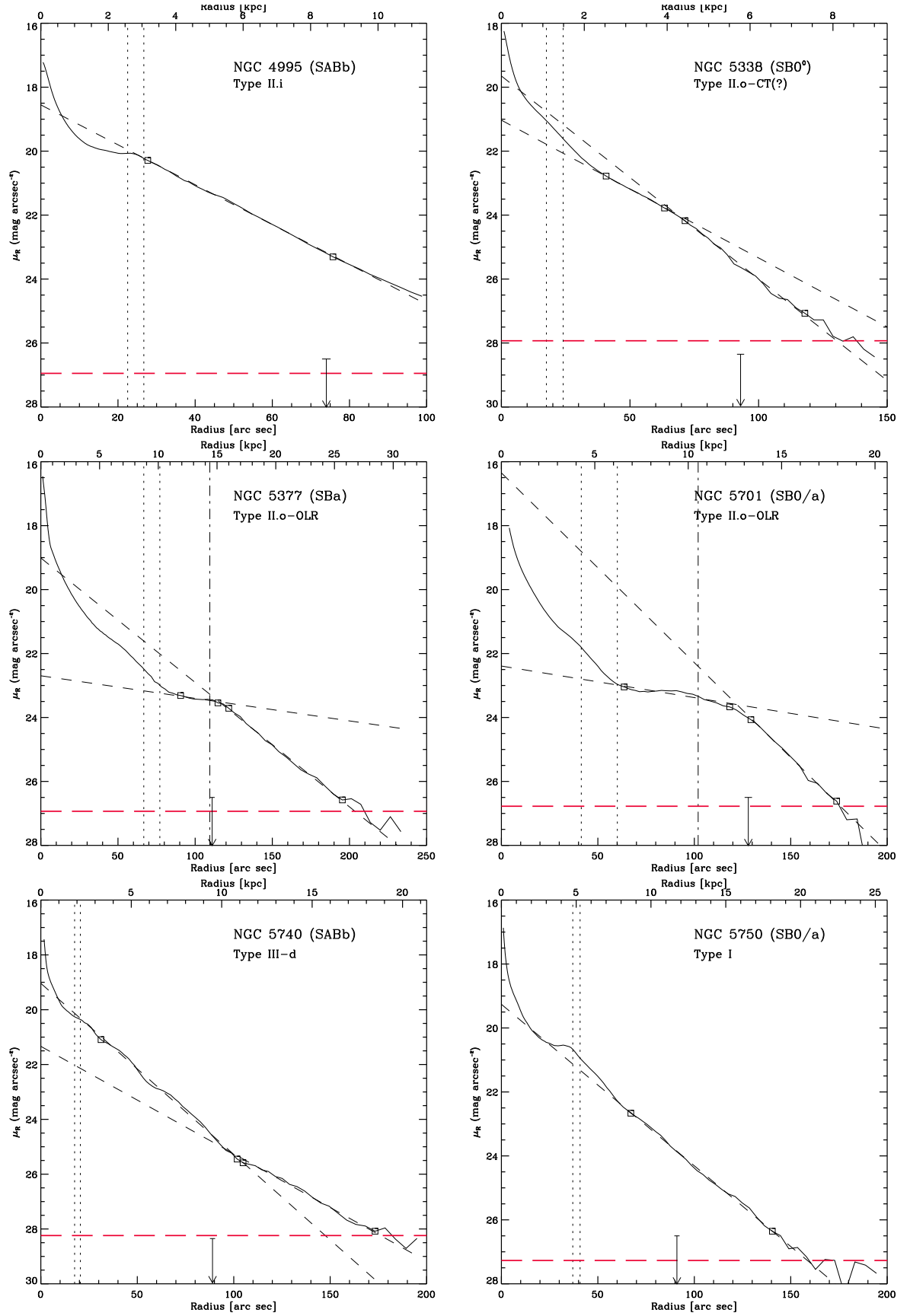


FIG. 14.— continued.

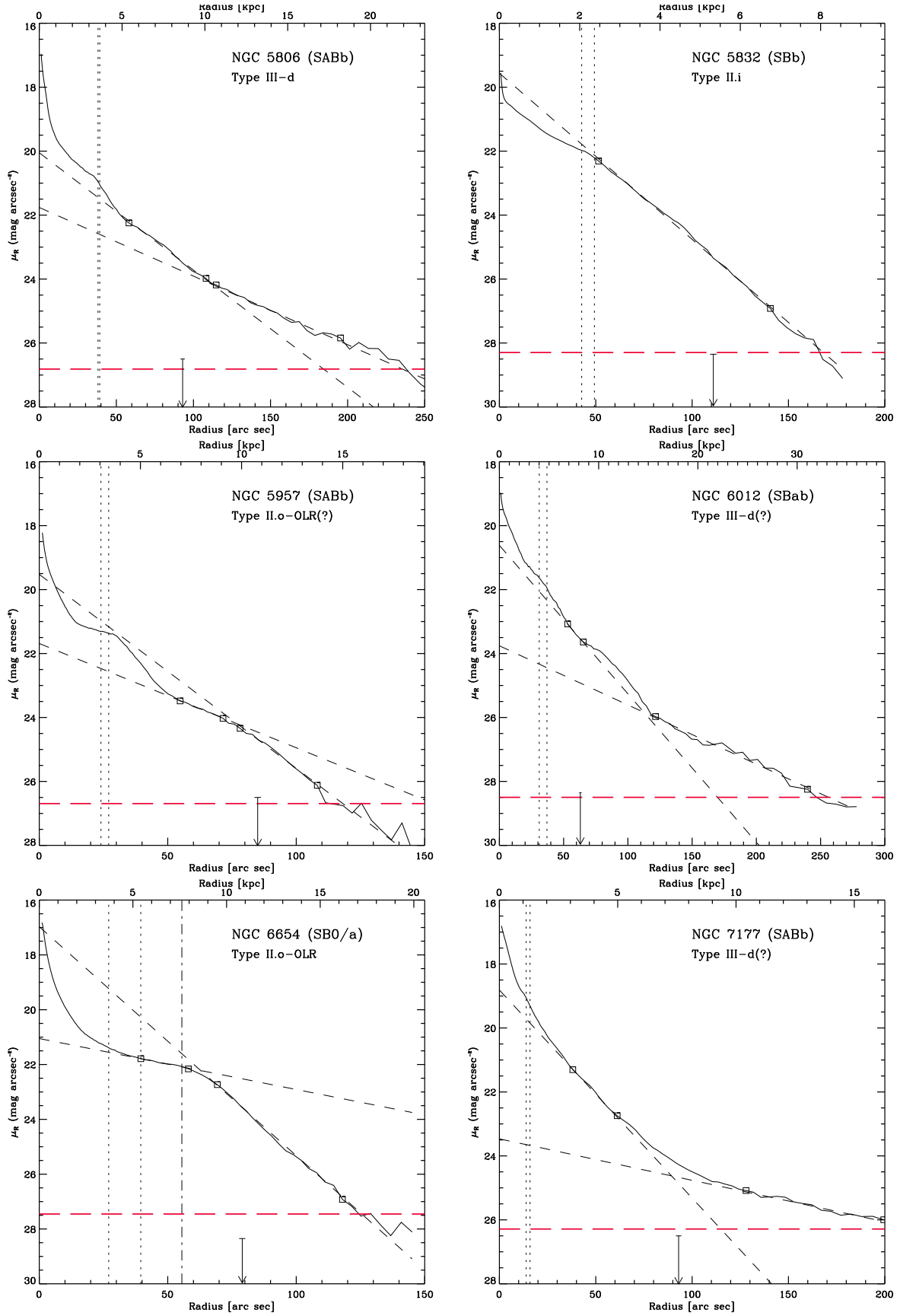


FIG. 14.— continued.

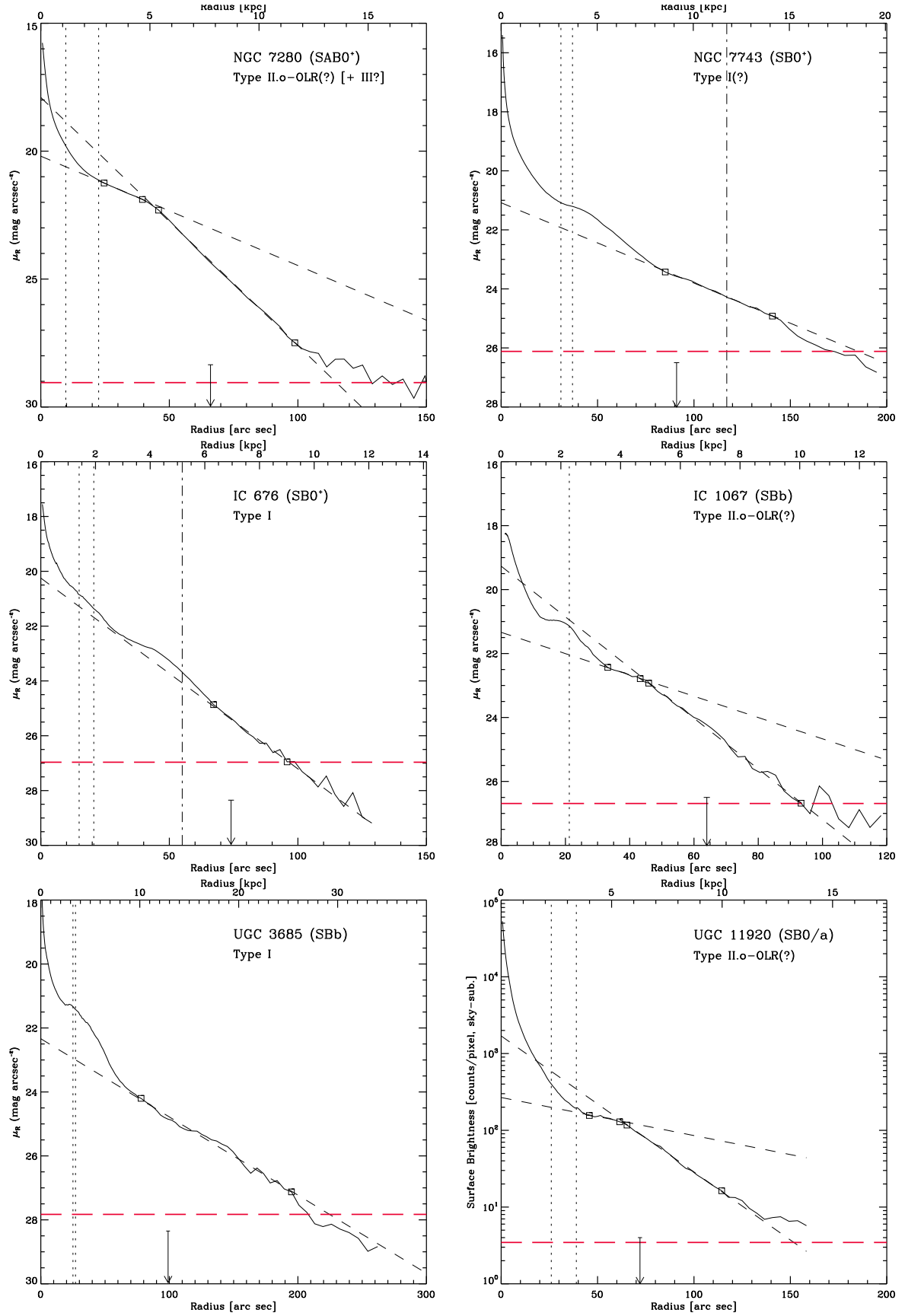


FIG. 14.— continued.